

# Estimating parameters and predicting membrane voltages with conductance-based neuron models

C. Daniel Meliza · Mark Kostuk · Hao Huang ·  
Alain Nogaret · Daniel Margoliash ·  
Henry D. I. Abarbanel

Received: 19 December 2013 / Accepted: 9 June 2014 / Published online: 25 June 2014  
© Springer-Verlag Berlin Heidelberg 2014

**Abstract** Recent results demonstrate techniques for fully quantitative, statistical inference of the dynamics of individual neurons under the Hodgkin–Huxley framework of voltage-gated conductances. Using a variational approximation, this approach has been successfully applied to simulated data from model neurons. Here, we use this method to analyze a population of real neurons recorded in a slice preparation of the zebra finch forebrain nucleus HVC. Our results demonstrate that using only 1,500 ms of voltage recorded while injecting a complex current waveform, we can estimate the values of 12 state variables and 72 parameters in a dynamical model, such that the model accurately predicts

the responses of the neuron to novel injected currents. A less complex model produced consistently worse predictions, indicating that the additional currents contribute significantly to the dynamics of these neurons. Preliminary results indicate some differences in the channel complement of the models for different classes of HVC neurons, which accords with expectations from the biology. Whereas the model for each cell is incomplete (representing only the somatic compartment, and likely to be missing classes of channels that the real neurons possess), our approach opens the possibility to investigate in modeling the plausibility of additional classes of channels the cell might possess, thus improving the models over time. These results provide an important foundational basis for building biologically realistic network models, such as the one in HVC that contributes to the process of song production and developmental vocal learning in songbirds.

**Electronic supplementary material** The online version of this article (doi:10.1007/s00422-014-0615-5) contains supplementary material, which is available to authorized users.

C. D. Meliza · H. Huang · D. Margoliash  
Department of Organismal Biology and Anatomy,  
University of Chicago, 1027 E 57th Street, Chicago, IL 60637, USA

*Present address:*

C. D. Meliza (✉)  
Department of Psychology, University of Virginia,  
PO Box 400400, Charlottesville, VA 22904, USA  
e-mail: cdm8j@virginia.edu

M. Kostuk  
Department of Physics, University of California, San Diego,  
9500 Gilman Drive, La Jolla, CA 92093-0402, USA

A. Nogaret  
Department of Physics, University of Bath, Claverton Down,  
Bath, UK

H. D. I. Abarbanel  
Department of Physics and Marine Physical Laboratory (Scripps  
Institution of Oceanography), Center for Theoretical Biological  
Physics, University of California, San Diego, 9500 Gilman Drive,  
La Jolla, CA 92093-0374, USA

**Keywords** Data assimilation · Neuronal dynamics · Ion channel properties · Song system

## 1 Introduction

Circuits of neurons typically comprise multiple cell types with distinct anatomical and physiological properties. Behaviors of circuits and organisms depend both on the intrinsic properties of component neurons and on the dynamics of their interactions. Many models for the emergence of complex behaviors in neurons and circuits are based on the formalism proposed by [Hodgkin and Huxley \(1952\)](#), which represents membrane dynamics in terms of ion currents through passive, voltage-gated, and ligand-gated conductances. The dynamics of these conductances can in turn be explained by biophysical properties of the specific ion channels expressed by the cell. These models can thus provide mechanistic insights into the

relationship between molecular cell properties and the emergence of complex behaviors (Briggman et al. 2005; Marder and Bucher 2007; Bean 2007b; Ayali and Lange 2010).

Tools for developing conductance-based models have matured in recent decades (Hines and Carnevale 1997; Herz et al. 2006; Gleeson et al. 2010), making it possible to realistically simulate large, complex networks. However, biophysical realism results in large numbers of free parameters related to the size and shape of compartments, the distribution and kinetics of ion channels, and the synaptic connections between neurons. Constraining these parameters with experimental data has proven to be a difficult problem for several reasons. First, although many kinds of ion channels have been identified and much is known about their biophysical properties (Trimmer and Rhodes 2004; Kew and Davies 2010), for all but a few well-studied classes of neurons (e.g., Kole et al. 2006), there are little data on which channels are expressed or their spatial distribution. Second, cellular morphology and the expression, isoform composition, and phosphorylation state of channels may vary widely among cells of the same type (Schulz et al. 2006; Günay et al. 2008) and over time (Cerda and Trimmer 2010; Johnston et al. 2010). Because of the nonlinear relationships between many parameters and membrane voltage, models based on parameter measurements averaged across cells may fail to reproduce the behaviors of individual neurons (Golowasch et al. 2002; Achard and Schutter 2006).

There have been numerous efforts to develop methods for inferring parameter values from the observed membrane voltage dynamics of individual neurons (Vanier and Bower 1999; Geit et al. 2008). The problem is one of optimization: Given a mathematical model of the system, find the set of parameters that most closely reproduces its behavior. For neural systems, the implicit problems of specifying the model and determining how to compare its behavior to the real system are far from trivial. Many mechanistic details can influence a neuron's responses within a circuit, and it is unclear what aspects of a neuron's response have functionally significant consequences. At the same time, the ability to consider models with more functional or mechanistic detail has been greatly limited by the optimization methods presently available. Approaches range from exhaustive grid, stochastic, and evolutionary search algorithms (Foster et al. 1993; Prinz et al. 2003; Druckmann et al. 2007; Reid et al. 2007; Hobbs and Hooper 2008; Buhry et al. 2012) to statistical inference procedures based on probabilistic frameworks that explicitly account for errors in measurement and model specification (Baldi et al. 1998; Huys et al. 2006; Huys and Paninski 2009; Lepora et al. 2011). These methods have been successful in estimating maximal conductance parameters, which is a linear problem, though channel kinetic parameters have proven more challenging, as this is a nonlinear problem (Pospischil et al. 2008; Hendrickson et al. 2011; Vavoulis et al. 2012).

Much progress has been made, but the current tools only support conductance models that are too simple to explain complex phenomena and often fail to give better predictions than phenomenological models (Jolivet et al. 2008a; Kobayashi et al. 2009).

We have previously described an exact statistical formalism for the problem of estimating the unknown states and parameters of conductance-based neuronal models given measurements of the membrane potential alone (Toth et al. 2011; Kostuk et al. 2012; Abarbanel 2013). In experiments with simulated data, we found that using an approximation to the exact formulation (Toth et al. 2011) and an interior-point optimization procedure (Wächter 2002), we could precisely estimate all the free parameters of a conductance-based model, including channel kinetic parameters. Here, we apply this method to whole-cell recordings in slices of the song premotor area HVC (a proper name) from zebra finches (*Taeniopygia guttata*). We chose this system in part because the component neurons fall into several well-defined classes with distinct functional roles within the larger song system. Models developed here can eventually be tested against the precisely timed patterns of activity that HVC emits during production of song (Hahnloser et al. 2002; Roberts et al. 2008; Long et al. 2010) and directly related to precise, analytic descriptions of the vocal behavior (Amador et al. 2013).

HVC comprises at least three broadly defined categories of neurons (Dutar et al. 1998): those projecting exclusively to striatal neurons in area X, those projecting exclusively to the motor cortex nucleus RA, and interneurons whose axons are confined to HVC. Each of these categories encompasses at least two subtypes (Nixdorf et al. 1989; Fortune and Margoliash 1995; Kubota and Taniguchi 1998; Shea et al. 2010), and there are likely to be more categories and subclasses of HVC neurons. Intracellular recordings *in vivo* and *in vitro* have defined principal attributes of the HVC circuit (Mooney 2000; Mooney and Prather 2005), but the relationship between the connectivity and intrinsic membrane properties of HVC neurons, and the production of song remain an active area of research (Jin et al. 2007).

Our goals were to test whether the methods developed on simulated data (Toth et al. 2011; Kostuk et al. 2012; Abarbanel 2013) also work with real neurons and if so, to determine whether the models give insight into the biology of HVC. Because the models are only an approximation to the physical system, and the true channel complements and kinetic properties are not known, we test the models by generating predictions to novel current injections and cross-validating against recorded responses. We find that with a sufficiently complex model, we can generate predictions for most neurons in HVC that are nearly as good as the intrinsic variability of the neurons. However, parameter estimates were highly variable across neurons and not strongly correlated with identified neuron types.

## 2 Results

### 2.1 Estimation and prediction of HVC neuron responses to injected current

We made whole-cell recordings from 26 HVC neurons and stimulated them in current-clamp by injection of a complex current waveform designed to close and open a broad range of voltage-gated ion channels with relatively short time constants. The observed voltage and the known injected current from 1,500 ms of the recording were used to estimate the unknown states and parameters of conductance-based dynamical models for each neuron. The completed model was then integrated forward to predict the response of the neuron to the remainder of the recording epoch.

Because the full complement of channels expressed by HVC neurons was not known, the model was developed iteratively, starting with a relatively simple model used in an earlier theoretical study (Toth et al. 2011). The initial model contained a transient sodium current (NaT), a noninactivating potassium current (K1), a hyperpolarization-activated cation current (HCN), and a passive leak current. Using a set of neurons that exemplified the range of physiological responses we observed, we compared the predictions of the models to the recorded voltages and added additional voltage-gated currents that might account for features of the response missing

from the prediction. Although calcium- and sodium-gated currents may be present in some classes of HVC neurons (Kubota and Saito 1991; Daou et al. 2013), their dynamics are complex and difficult to infer from limited amounts of data, so they were not explored in this analysis (see Sect. 3). The predictions in each iteration were evaluated using spike shape, spike rate, and the root-mean-square (RMS) deviation in the subthreshold voltage. The final model included a persistent sodium current (NaP), an inactivating potassium current (K2), a slow noninactivating potassium current (K3), a high-threshold L-type calcium current (CaL), and a low-threshold T-type calcium current (CaT), with a total of 12 state variables and 72 free parameters. These currents are not meant to represent a specific type of ion channel that has been identified in HVC neurons. Each of these currents, however, can represent a composite of ion channels that share the same or similar gating kinetics. Actual HVC neurons may contain a subset of the ion channels that are well modeled by these currents and may contain additional ion channels that are poorly modeled by these currents.

We highlight three example neurons. Two of the neurons, which showed little or no adaptation to step currents, were likely to be X-projecting (hereafter, N1 and N2) (Figs. 1c, 2c). The third, which showed rapid adaptation to step currents, was likely to be RA-projecting (N3) (Fig. 3c). The measured

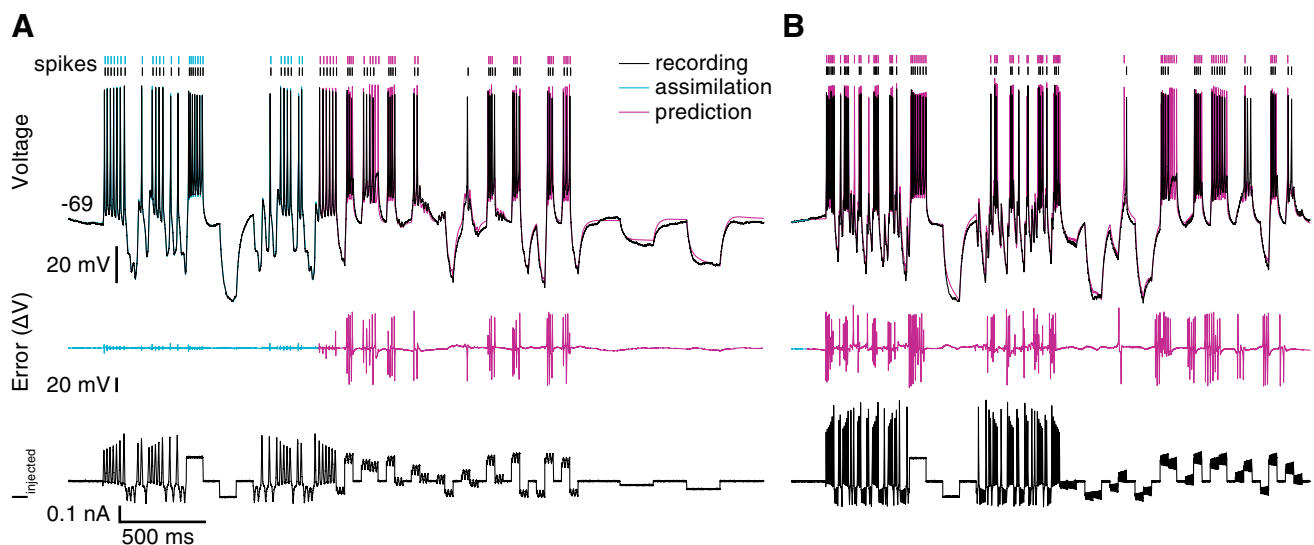


**Fig. 1** Data assimilation window and prediction window for intracellular responses for exemplar neuron N1. **a** Membrane voltage (top) in response to injection of a complex current waveform (bottom). The black trace shows recorded voltage, and the cyan trace shows estimated voltage from the data assimilation procedure for times between 0–1,500 ms, during which all state variables and parameters of the model were estimated. The magenta trace shows the voltage predicted by integrating the completed model with estimated parameters and state variables forward in time beyond 1,500 ms. Vertical tick marks above the voltage trace indicate times of action potentials in the recorded data

(black), estimations (cyan), and predictions (magenta). The numeric value at the beginning of the voltage trace represents the initial datum of the recorded voltage (in mV). The middle plot shows the error in voltage estimates (cyan) and predictions (magenta) relative to the recording. **b** Cross-prediction of model in **a** to a later recording epoch with a different injected current. The parameters from **a** were held constant, while a brief assimilation period (cyan) (100 ms) was used to set initial conditions before generating the prediction (magenta) (color figure online)

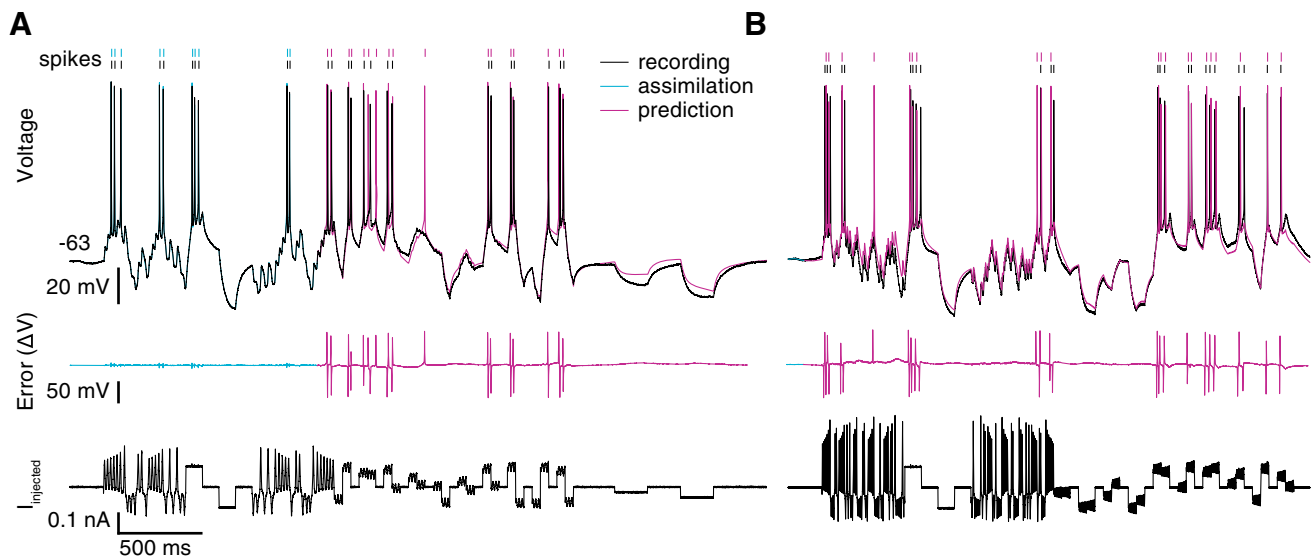


**Fig. 2** Data assimilation window and prediction of intracellular responses for exemplar N2. The format is the same as in Fig. 1. Note the differences with N1 in membrane time constant, lower firing rate, and reduced after-spike hyperpolarization. In all panels, black traces are recorded values, cyan traces are estimates obtained during the data

assimilation, and magenta traces are predictions from the completed model. **a** Membrane voltage (*top*) in response to current injection (*bottom*), with errors in estimates and predictions (*middle*). **b** Membrane voltage (*top*) in response to different current stimulus (*bottom*) (color figure online)

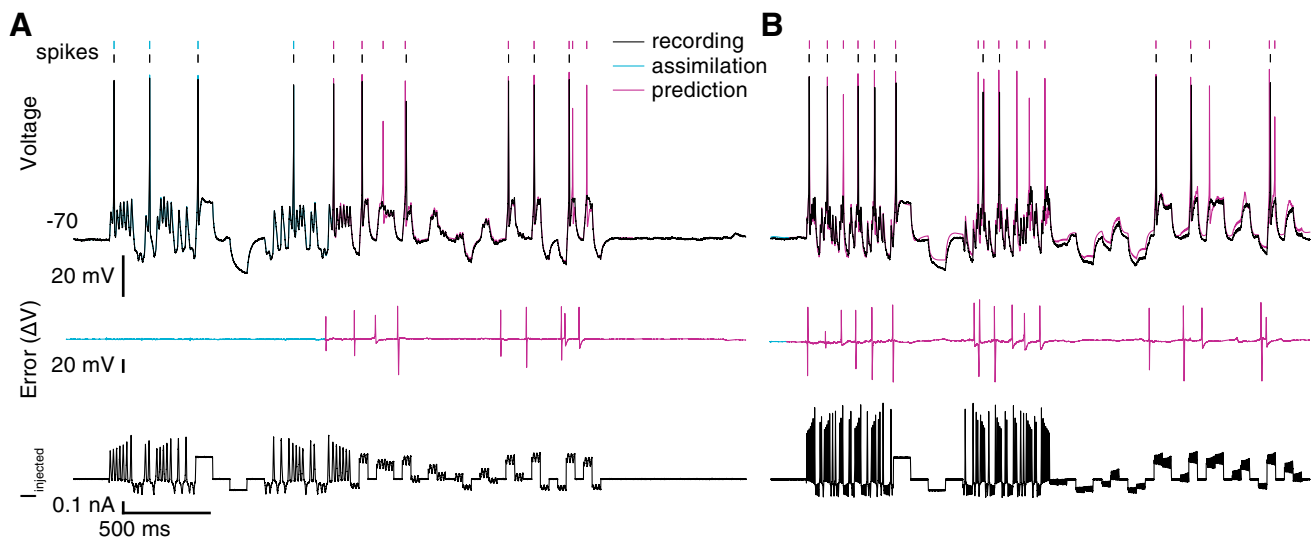


**Fig. 3** Data assimilation window and prediction of intracellular responses for exemplar N3. The format is the same as in Fig. 1. Note the much lower spike rate and strong adaptation compared to N1 and N2. In all panels, black traces are recorded values, cyan traces are estimates obtained during the data assimilation, and magenta traces are predic-

tions from the completed model. **a** Membrane voltage (*top*) in response to current injection (*bottom*), with errors in estimates and predictions (*middle*). **b** Membrane voltage (*top*) in response to different current stimulus (*bottom*) (color figure online)

voltage trace and injected current used to complete the neuron model for each of the exemplar neurons are shown in Figs. 1a, 2a and 3a. The recorded voltage trace is shown in black, and the final estimated  $V_m(t)$  of the model is in cyan. The magenta traces show the results of integrating the completed model forward using the estimated values of the parameters and

state variables at the end of the assimilation window and the known injected current.

To further validate the model, a prediction for a different recording epoch was created, using a short (100 ms) assimilation window to estimate only the unobserved state variables (giving us the initial conditions of the channel gat-

ing particles), while the previously obtained parameters were held fixed. The model was then integrated forward with the known injected current to predict the response to the rest of the epoch (Figs. 1b, 2b and 3b). One additional parameter  $I_{dc}$  was optimized for the prediction, which compensated for drifts in membrane potential between the parameter assimilation epoch and the inter-epoch prediction.

For both the intra- and inter-epoch predictions, the predicted responses reasonably matched the recordings in terms of spike rate, spike timing (compare black tick marks for recorded data to colored tick marks for model data in Figs. 1, 2 and 3), and subthreshold voltage. Predicted spike times did not always align perfectly with spikes in the data, as indicated by large excursions in the error between the predicted and recorded voltage (e.g., Fig. 1a, middle plot). However, this variation was comparable to what we observed in measured responses to the same stimuli presented at different times (data not shown). Similarly, errors in the predicted responses to hyperpolarizing currents were consistent with small variations in input resistance over the time course of the recording.

The models reproduced many fine levels of detail in the recordings. Predicted spikes from the models closely matched the shape of the spikes in the recordings (Fig. 4), with the exception of a rapid depolarization “kink” visible in the phase plane plots of the spikes for N1 and N2.

We also tested the models on their ability to predict responses to step currents (Fig. 5). The models accurately predicted some features of these responses (for example, neuron 3 exhibited a slight overshoot when depolarized), but made errors on other features, including the relationship of current to firing rate (Fig. 5b). These errors may reflect the fact that long step currents were not used in data assimilation (see Sect. 3).

## 2.2 Estimated currents and channel kinetics

A detailed view of the estimated currents and gating state variables during the data assimilation window is shown for neurons N1, N2, and N3 in Figs. 6, 7 and 8, respectively. As expected, the neurons showed a strong dependence upon the fast sodium current and a potassium current for spike generation, but subtle differences in the strength and kinetics of these currents led to differences in spike shape and excitability. Compared with N2, N1 (Fig. 6) had a higher spike rate, a stronger after-hyperpolarization potential (AHP), and little to no change in spike shape or rate with prolonged depolarization (i.e., adaptation). In the model, these differences were due to a relatively stronger potassium current in N1, which repolarized the cell more rapidly and strongly. In the model for N2 (Fig. 7), the K current was weaker and somewhat slower, leading to a weaker AHP but also to a buildup of NaT inactivation, which may have accounted for changes in spike shape and rate over sustained depolarization.

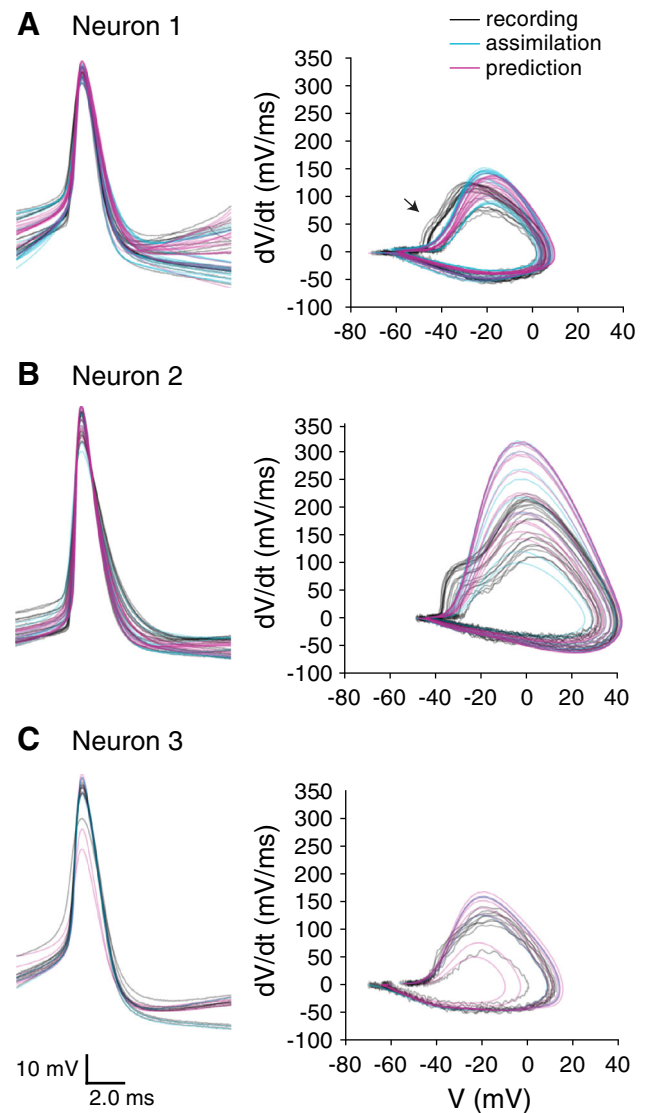
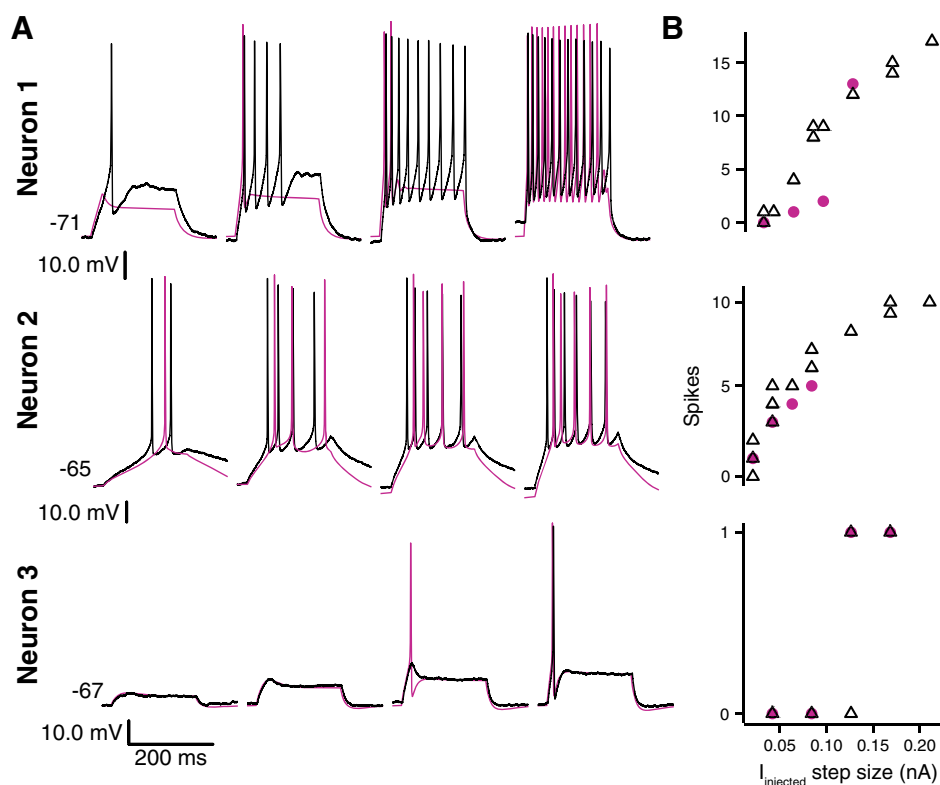


**Fig. 4** Recorded and model spike shapes for the three exemplar neurons. *Left panels* show randomly selected spikes extracted from the recorded voltage (*black*), assimilation estimates (*cyan*), and model predictions (*magenta*). *Right panels* show the same spikes plotted in the phase plane, which reveals additional details of the spike shape. Each spike appears as a loop, with increasing time going clockwise. The *arrow* indicates an initial period of rapid depolarization not captured by the model (color figure online)

As with N1, the model for N3 (Fig. 8) had a strong K current that resulted in a pronounced AHP. However, this current was supplied by a channel with  $m^1$  kinetics, which caused it to stay open during prolonged depolarizations. This current was balanced by a positive current from the persistent sodium channel. Together, these currents provided strong shunting inhibition that prevented the model from firing more than one action potential and gave it its phasic response properties.

The relative importance of each of the currents in the model was ascertained in two ways. The first was to com-

**Fig. 5** Recorded and model responses to step depolarizations. **a** Recorded voltage (*black*) and model predictions (*magenta*) of the three exemplar neurons in response to a series of depolarizing step currents. **b** Number of spikes observed during 200 ms depolarization as a function of step size. *Open triangles* indicate recorded responses. *Magenta filled circles* indicate model predictions (color figure online)



pare the maximal conductances, both directly (Table 1) and as a fraction of the total membrane conductance ( $\tilde{g}_\alpha = g_\alpha / \sum_i g_i$ , Fig. 9a). As noted above, the N2 model had strong NaT conductance and relatively weak K conductances, accounting for its rapid depolarization (Fig. 4b) and weak AHP. For N3, the dominant potassium conductance was from K3.

Categorizing neurons based upon their channel maximal conductances  $g_\alpha$  may not accurately reflect the dynamical importance of the channels in driving the membrane voltage over a significant time interval. It is not the maximal conductance, but the strength of the current that influences changes in the membrane voltage. Small subthreshold conductances may have large effects on neuron behavior if they are active over long timescales and generate large currents averaged over time. Thus, the second method we used to identify important currents was to calculate the fraction of the total time-averaged current from each channel type  $\alpha$ ,  $\tilde{I}_\alpha = \left\langle \frac{|I_\alpha|}{\sum_i |I_i|} \right\rangle_T$ . These values are shown in Fig. 9b. The absolute value was used so that the comparison was relative to the magnitude of the total ion flux, and the time average was taken over the data assimilation window,  $T$ . Comparing  $\tilde{I}$  values across neurons reveals the contribution of NaP to N3 dynamics, CaT to N2 dynamics, and K3 to the dynamics of all three neurons, effects that are not

seen in the maximal conductances because these channels were weakly but tonically active. Conversely, the NaT currents were strongly expressed in terms of  $\tilde{g}$ , but their rapid opening and closing resulted in a diminished contribution to the total neuronal current. The  $\tilde{I}$  values were not corrected for differences in the number of action potentials produced during the assimilation period, which would influence the relative contribution of spike-generating and subthreshold currents.

Additional differences among neurons were also seen in the parameters governing channel dynamics. Figure 9c shows the equilibrium state ( $x_\infty(V)$ ) and relaxation time constant ( $\tau(V)$ ) as a function of voltage for the activation and inactivation variables for several channels. The K3 channel in the model for N3 had a higher  $V_{1/2}$  relative to both the same channel in the other neurons and relative to the  $V_{1/2}$  of the K2 channels in the N1 and N2 models (Fig. 9c). This feature allowed some proportion of the K3 channels to remain open in moderately depolarized conditions, possibly contributing to the phasic response properties of this neuron. Also for N3, the  $V_{1/2}$  parameter for NaT inactivation was low relative to the other two neurons, leading to a shift in the time-constant function and slower kinetics at hyperpolarized potentials. Thus, the NaT current remained inactivated longer in the N3 model, possibly contributing to this neuron's phasic responses.

**Fig. 6** Estimated ion currents from the completed model for exemplar N1. **a** Voltage response to complex current injection. Note the after-spike hyperpolarization, consistent spike height, and minimal adaptation. **b** Currents from the major fast sodium and potassium channels from the model. Only the fast sodium (NaT) and inactivating potassium (K2) currents contribute significantly to spike generation. **c** Estimated values for the NaT activation (*solid blue line*) and inactivation (*dashed blue line*) gating variables, and the K2 activation and inactivation gating variables (*cyan lines*). The full range from 0 to 1 is shown. **d–f** Details of voltage, current, and gating variable estimates for the spike indicated by an arrow in **a** (color figure online)

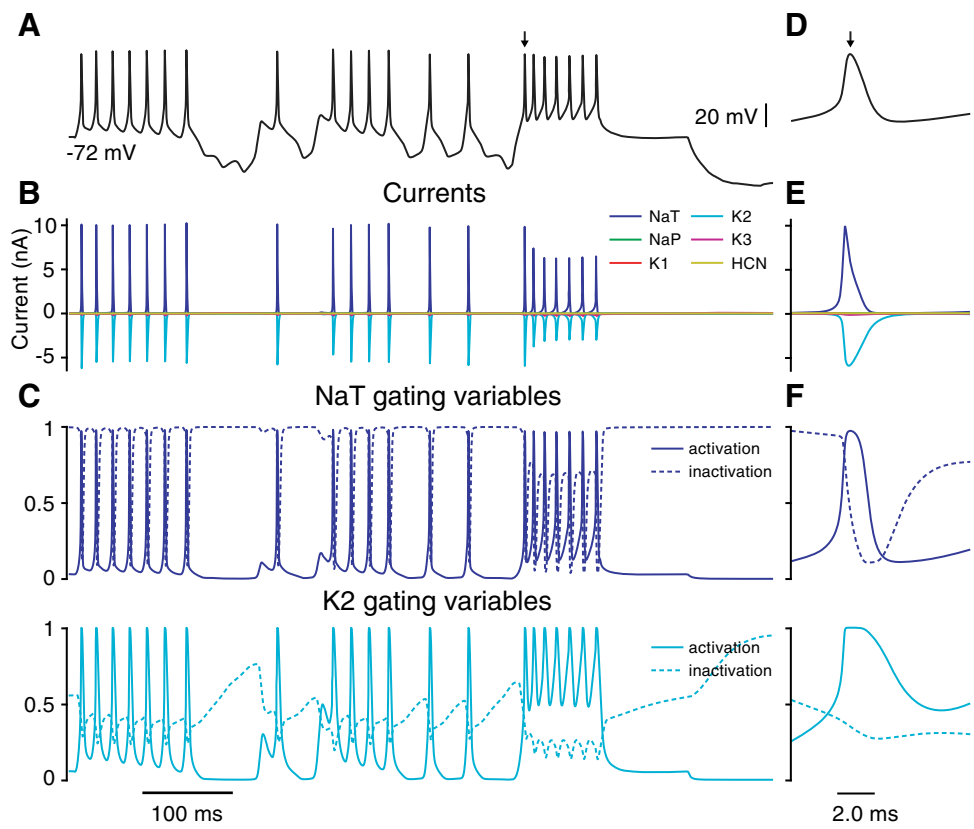


**Fig. 7** Estimated ion currents from the completed model for exemplar N2. The format is the same as in Fig. 6. Similar to N1, only the fast sodium (NaT) and inactivating potassium (K2) currents contribute significantly to spike generation, but note the relatively stronger NaT vs K2 current and the buildup of inactivation during long depolarizations that leads to spike rate and shape adaptation. **a** Voltage response to current injection. **b** Estimated currents from the completed model. **c** Estimated values for NaT activation and inactivation gating variables and the K2 activation and inactivation variables. **d–f** Details of voltage, current, and gating variable estimates for the indicated spike in **a**

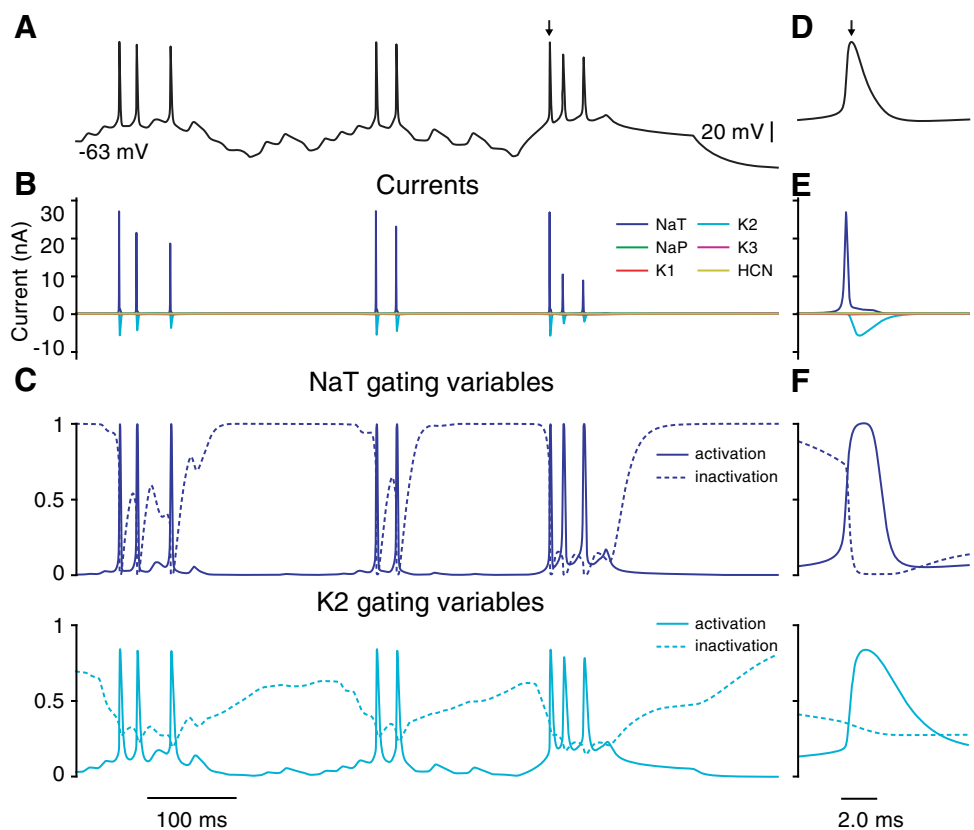


**Fig. 8** Estimated ion currents from the completed model for exemplar N3. The format is the same as in Fig. 6. Differing from N1 and N2, the slow, noninactivating potassium (K3) current drives repolarization and remains open during prolonged depolarization. Also note the slight presence of the NaP current between spikes. **a** Voltage response to current injection. **d** Estimated currents from the completed model. **c** Estimated values for NaT activation and inactivation gating variables, NaP activation variable, and K3 activation variable. **d–f** Details of voltage, current, and gating variable estimates for the indicated spike in **a**

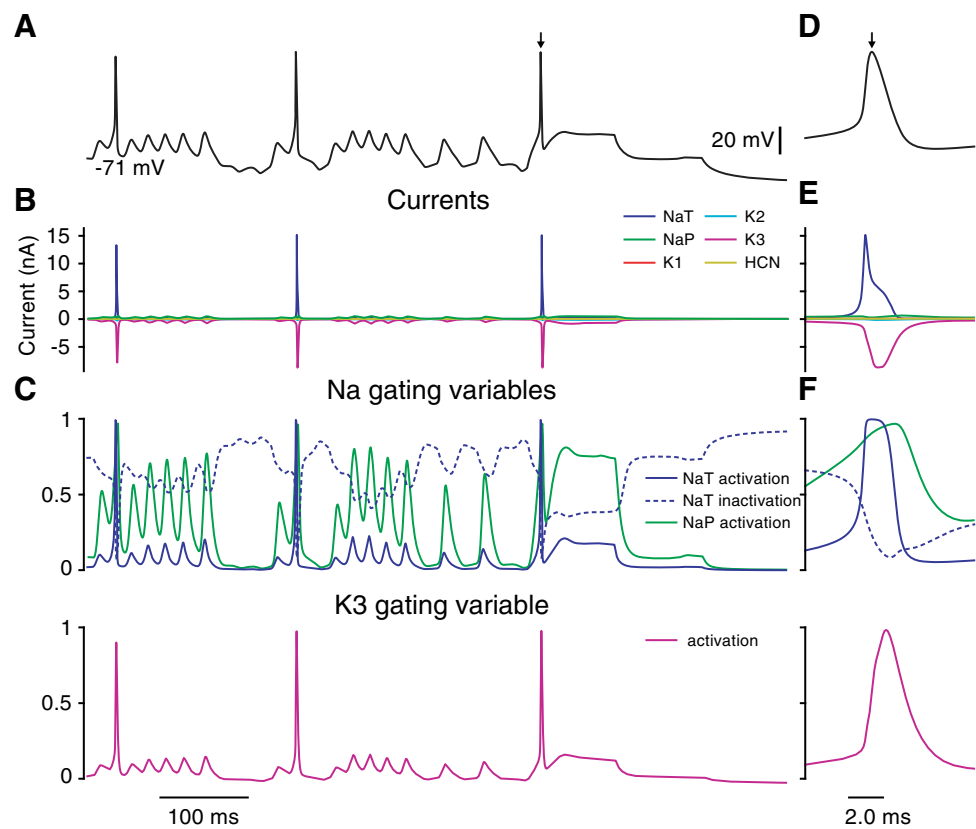


**Table 1** Conductance parameter estimates and optimization bounds for exemplar neurons N1–N3

| Param. number | Param. 'name' | Lower bound | Upper bound | Neuron N1 | Neuron N2 | Neuron N3 |
|---------------|---------------|-------------|-------------|-----------|-----------|-----------|
| $p_9$         | Leak          | 0.010       | 0.600       | 0.010     | 0.036     | 0.047     |
| $p_2$         | NaT           | 5.000       | 170.000     | 7.545     | 85.364    | 9.736     |
| $p_3$         | NaP           | 0.000       | 20.000      | 0.008     | 0.086     | 0.075     |
| $p_5$         | K1            | 0.000       | 80.000      | 0.096     | 0.216     | 0.000     |
| $p_6$         | K2            | 0.000       | 80.000      | 5.687     | 14.708    | 1.074     |
| $p_7$         | K3            | 0.000       | 12.000      | 0.438     | 0.191     | 6.482     |
| $p_{12}$      | HCN           | 0.000       | 10.000      | 0.017     | 0.011     | 0.000     |
| $p_{71}$      | CaL           | 0.000       | –           | 0.000     | 0.012     | 0.000     |
| $p_{72}$      | CaT           | 0.000       | –           | 0.000     | 0.003     | 0.005     |

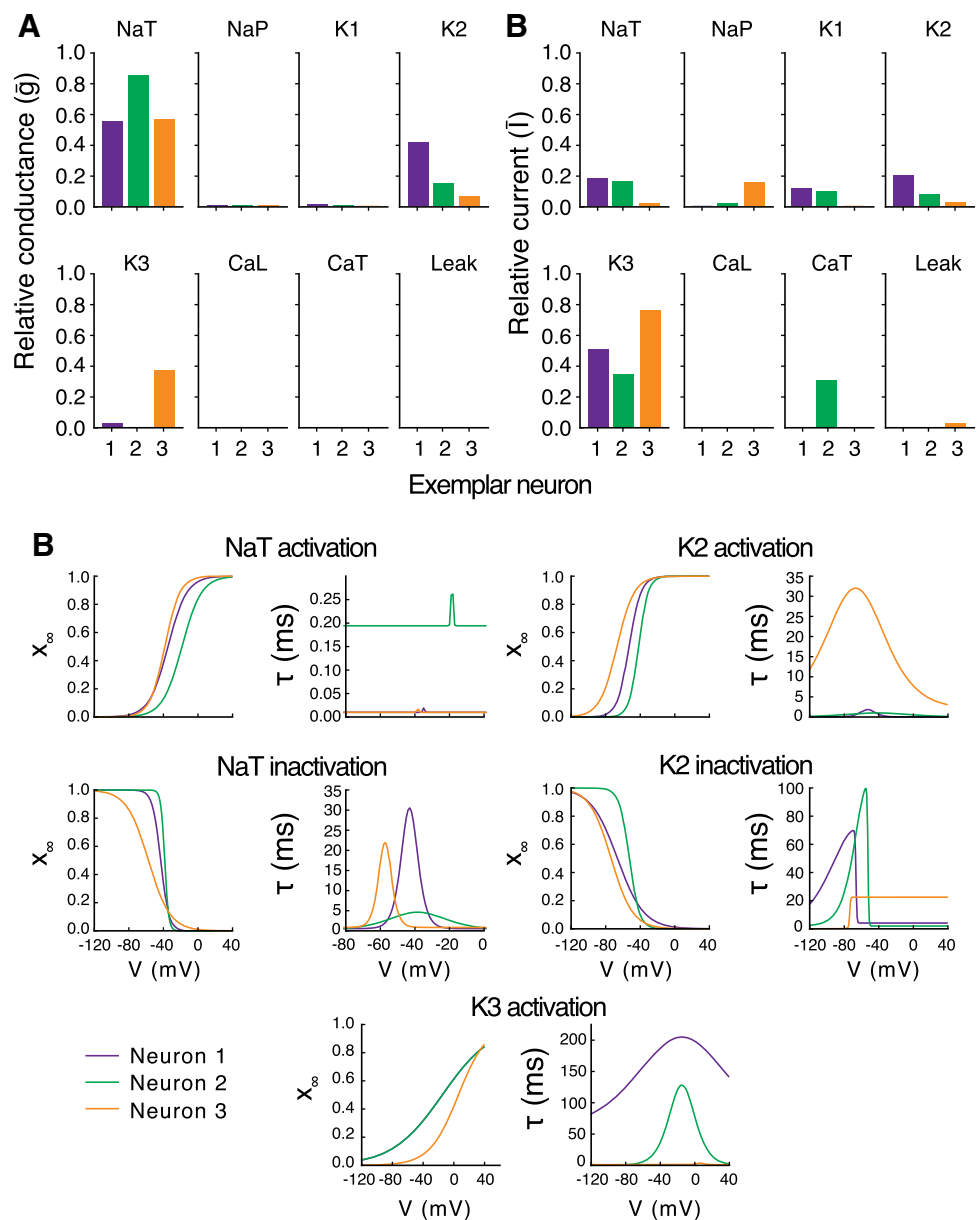
All units are  $\text{nS}/\text{cm}^2$ . Permeabilities for the calcium channels were converted to conductances by evaluating the GHK expression with the estimated calcium concentrations and  $V = 0$  mV (upper bounds are not shown for calcium channel conductances because they depend on multiple parameters). See Table S1 for the complete list of parameter estimates

### 2.3 Posterior distribution of parameter estimates

The parameter and state estimates obtained through the variational method are point estimates representing the values most likely to give rise to the data. To explore the posterior variance (i.e., uncertainty) of these estimates, we generated sampling distributions using a Metropolis-Hastings Monte Carlo algorithm (see Sect. 4.6 and Kostuk et al. 2012). The marginal posterior distributions of selected parameters

from the three exemplar neurons are shown in Fig. 10. Some parameters were strongly constrained by the data, such that only a narrow range of values was consistent with the observed response, whereas other parameters had broader distributions. Several of the parameters had complex, multimodal distributions. Note that the graphs only show distributions for single parameters and cannot indicate whether some combinations of parameters are particularly probable.

**Fig. 9** Comparison of currents and channel kinetics for exemplar neurons. **a** Maximal conductances relative to the total conductance or average current for each of the major currents in the model, for neurons N1, N2, and N3.  $I_{HVCN}$  is not shown as it did not contribute significantly to any of the models. **b** Average current contribution for each of the major currents in the model relative to the total average current. **c** Kinetics of the activation and inactivation variables for NaT and K2 currents, and activation variables for K3 currents for the exemplar neurons shown in terms of their equilibrium activation  $x_{\infty}(V)$  and relaxation time  $\tau(V)$



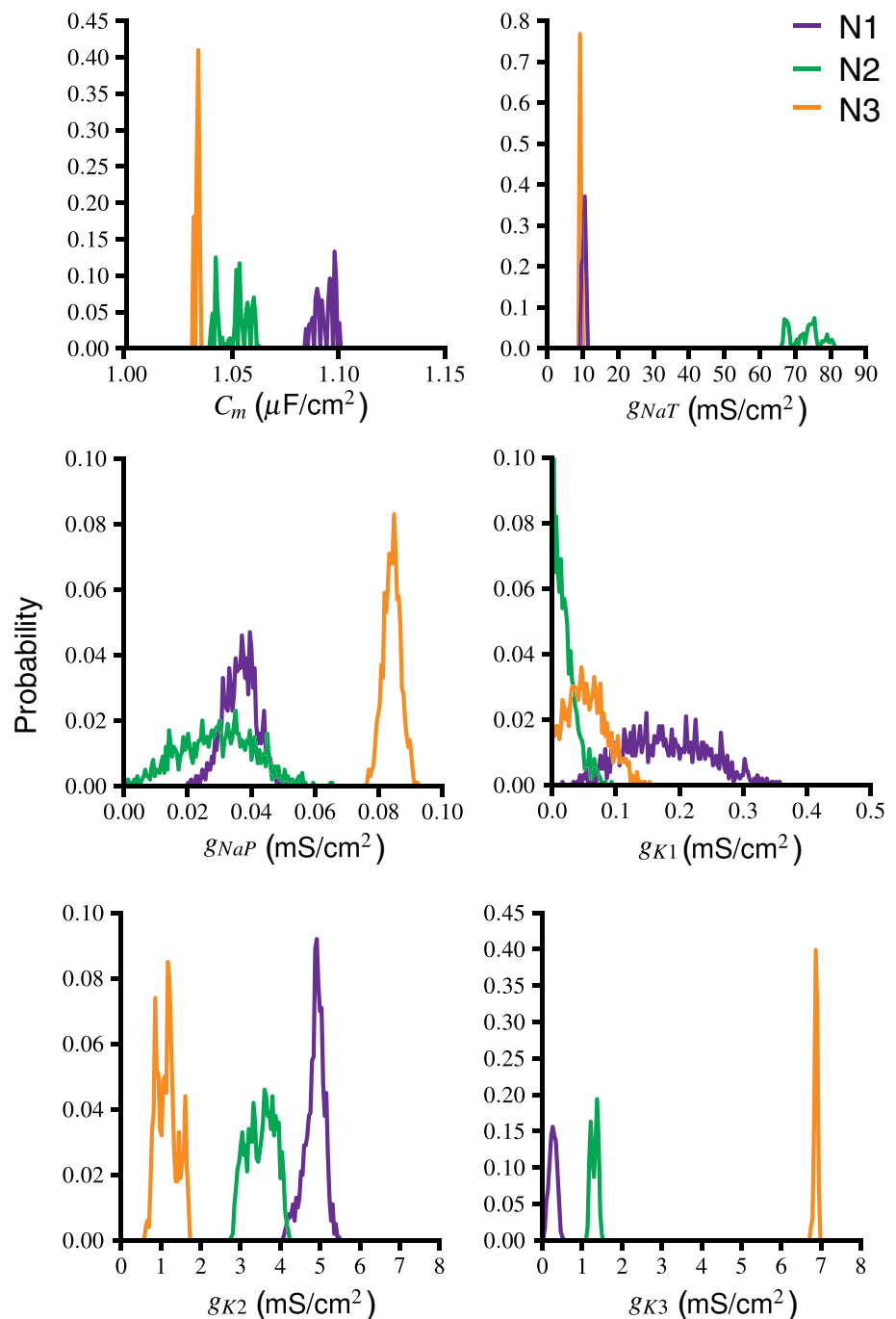
### 2.4 Model validation and selection

After the exemplar neurons were characterized, the final form of the model was used in data assimilation for all 26 neurons in the recorded population. For each neuron, three recording epochs with different stimulation waveforms were chosen. The stimulation protocols were similar across neurons except in amplitude, which was adjusted during the experiment to ensure sufficient numbers of action potentials. Each completed model was used to generate an intra-epoch prediction (as in Fig. 1a), which was compared to the data using metrics for similarity of subthreshold voltage, spike rate, spike shape, spike timing, and total correlation (see Sect. 4.5). Of the five metrics, the spike timing is

likely to have the most relevance to the function of HVC in song.

There was substantial variability within neurons in prediction quality. Often, models estimated from different epochs reproduced different features of the response better than others. Therefore, for each neuron, we picked the model that gave the best overall performance across all the prediction metrics. Table 2 shows summary statistics of the prediction metrics for all the models and for the best-ranked models for each neuron. It also shows summary statistics for intrinsic variability, which was measured by comparing for each neuron its responses to repeated presentations of the same stimulus (see Sect. 4.5). As quantified by these metrics, the differences between best model predictions and neural responses

**Fig. 10** Posterior distributions of selected parameters. The uncertainty in the reported parameter solution set for the membrane capacitance  $C_m$  and maximal conductances of neurons N1 (purple), N2 (green), and N3 (orange). Using a Metropolis-Hastings Monte Carlo algorithm, the distribution was sampled with the variational method estimates for initial guesses (color figure online)



are comparable to differences between neural responses to the same injected current. In some cases, the intrinsic deviance was higher than the model deviance, although this is likely to reflect small, slow changes in input resistance over the course of the recording.

One possible explanation for high within-neuron variability in model quality is that different stimuli explored different regions of the model state space, leading to solutions that emphasized some features more than others. We made a more extensive analysis of prediction quality using many

sets of data from the three exemplar neurons. For each neuron, we selected 26–28 recording epochs, and from each epoch between 1–3 (mean 2.6) overlapping segments of data to assimilate. Predictions for each completed model were compared to unassimilated data, and the variance in prediction quality between epochs was compared to the variance within epochs (Figure S1). For three of the five metrics, between-epoch variance was significantly higher than within-epoch variance (F-test; spike shape:  $F_{39,152} = 2.85$ ,  $P = 2.7 \times 10^{-6}$ ; spike timing:  $F_{41,163} = 3.36$ ,  $P =$

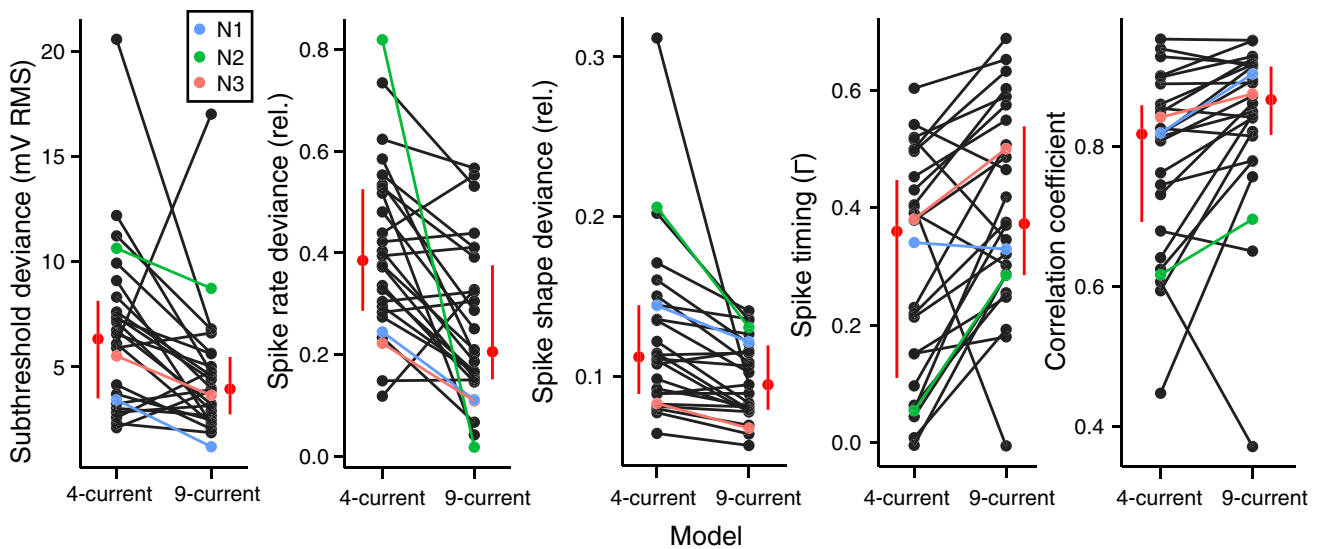


**Fig. 11** Comparison of simple and complex model prediction quality. Each panel shows one of the metrics of how well models predicted various features of the intracellular voltage trace. Points connected by lines correspond to individual neurons and show scores averaged from the three assimilation epochs. For deviance metrics, smaller values indicate closer agreement with recorded data, whereas for correlation coefficient,

larger values indicate better agreement. Blue, green and red dots correspond to exemplar neurons. Red dots displaced to either side indicate median values, and vertical bars the 25th and 75th percentiles. The 9-current model is significantly better for all metrics (paired Wilcoxon test: all  $P < 0.003$ ) (color figure online)

**Table 2** Prediction quality metrics for models of 26 HVC neurons

| Metric                         | All Models <sup>a</sup> |                  |                            |                           | Best Models <sup>b</sup> |             | Intrinsic |             |
|--------------------------------|-------------------------|------------------|----------------------------|---------------------------|--------------------------|-------------|-----------|-------------|
|                                | Median                  | IQR <sup>c</sup> | $\sigma_{\text{neuron}}^d$ | $\sigma_{\text{epoch}}^e$ | Median                   | IQR         | Median    | IQR         |
| subthreshold deviance (mV)     | 3.5                     | 2.3–5.3          | 5.4                        | 4.8                       | 2.6                      | 1.7–3.8     | 5.9       | 4.7–6.8     |
| spike rate deviance            | 0.22                    | 0.049–0.38       | 0.27                       | 0.24                      | 0.09                     | 0.00–0.26   | 0.13      | 0.10–0.21   |
| spike shape deviance           | 0.087                   | 0.070–0.13       | 0.041                      | 0.042                     | 0.077                    | 0.060–0.096 | 0.061     | 0.052–0.087 |
| spike coincidence ( $\Gamma$ ) | 0.38                    | 0.25–0.57        | 0.29                       | 0.23                      | 0.45                     | 0.32–0.69   | 0.52      | 0.39–0.61   |
| correlation coefficient        | 0.87                    | 0.80–0.92        | 0.21                       | 0.10                      | 0.88                     | 0.84–0.92   | 0.84      | 0.82–0.89   |

Multiple models for each neuron were estimated with data from different recording epochs. The left columns show summary statistics for all the models; the central columns show statistics for the best model; and the right columns show statistics comparing measured responses of individual neurons to repetitions of the same stimulus ( $n = 18$  neurons, mean epochs per neuron  $\pm$  SD =  $2.4 \pm 0.7$ ). IQR: interquartile range

<sup>a</sup>Statistics for all neurons and epochs

<sup>b</sup>Statistics for the 26 best models, one for each neuron

<sup>c</sup>Interquartile range (i.e., 25th and 75th percentile)

<sup>d</sup>Sample standard deviation between neurons

<sup>e</sup>Sample standard deviation between epochs from the same neuron

$2.4 \times 10^{-8}$ ; correlation:  $F_{41,163} = 1.50$ ,  $P = 0.041$ ; spike rate:  $F_{41,163} = 1.46$ ,  $P = 0.05$ ; subthreshold deviance:  $F_{41,163} = 1.14$ ,  $P = 0.28$ ), suggesting that differences in current stimulus had an effect on model quality.

To determine whether the additional currents in the model quantitatively improved predictions, the assimilation and prediction procedures were also applied to the same data using the initial model, which had only three voltage-gated conductances. By all measures, the more complex model produced better predictions (Fig. 11). In a pairwise compari-

son between simple and complex models estimated from the same data, the median difference in subthreshold deviance was 1.46 mV (paired Wilcoxon test:  $P = 2.7 \times 10^{-5}$ ), in spike rate deviance, 0.14 ( $P = 5.8 \times 10^{-5}$ ), in spike shape deviance, 0.015 ( $P = 2.6 \times 10^{-4}$ ), in spike coincidence, 0.11 ( $P = 3.2 \times 10^{-5}$ ), and in correlation coefficient, 0.036 ( $P = 3.7 \times 10^{-5}$ ). For 21/26 neurons (81%), the complex model produced the best overall prediction. Four of the neurons better predicted by the simpler model were putatively RA-projecting, and one was a putative interneuron.

## 2.5 Comparison of parameter estimates across cell types

We obtained a large enough sample of putative X-projecting ( $n = 7$ ) and RA-projecting neurons ( $n = 16$ ) to compare parameter estimates within and between these cell types. We selected the best model for each neuron and compared parameter estimates across the population. For the neuron's better fit by the simpler model, the conductances of the omitted channels were assumed to be zero. Some parameter values were consistent across the population, some differed significantly between putative cell types, and others were highly variable without any obvious correlation to physiology. As shown in Fig. 12a, relative maximal conductance and current contribution for the HCN current was low for almost all the neurons, which is consistent with the lack of an obvious sag current in responses to hyperpolarization (see Sect. 3). Similarly to the exemplar neurons, CaT and CaL relative conductances were close to zero for all the neurons, whereas the relative current contribution from calcium channels was substantial, accounting for  $12 \pm 2\%$  (mean  $\pm$  SEM) of the total current.

For the subset of neurons identified as RA-projecting based on their phasic response properties, relative NaT conductance was significantly lower than in putative X-projecting neurons (Wilcoxon test,  $P = 0.006$ ). This difference may correspond to the relatively higher excitability of X-projecting neurons. As noted above, maximal conductances do not fully reflect the dynamical importance of a current over time, but may indicate structural differences between neurons related to channel expression levels. Within each of the putatively classified groups of neurons, there was substantial variability in conductance levels.

Kinetic parameter estimates also varied substantially across neurons, and we were unable to discern any obvious clustering that might correspond to specific cell types. As an example, estimates for the kinetic parameters that define the transient sodium channel are shown in Fig. 12b. The activation and inactivation variables are each governed by four parameters: the half-potential  $V_{1/2}$  and slope  $\kappa$  of the equilibrium activation  $x_{\infty}(V)$ , and the width  $\sigma$  and peak height  $\tau_{\max}$  of the relaxation time constant  $\tau(V)$ . Most of the estimates for the parameters associated with  $x_{\infty}(V)$  were well within the bounds specified in the assimilation procedure, suggesting that these parameters are well constrained by the data; in contrast, many of the estimates for the parameters associated with  $\tau(V)$  were at or near the bounds. It may be difficult to reliably estimate time constants from current-clamp data because the neuron does not stay at highly depolarized voltages for very long.

## 3 Discussion

These results demonstrate the application of a statistical method for estimating unknown states and parameters of complex, conductance-based, dynamical neuron models. Using this method, which is a variational approximation to the high-dimensional path integral relating measured voltage to the internal dynamics of voltage-gated ion channels (Toth et al. 2011; Abarbanel 2013), we obtained state and parameter estimates for models of individual neurons from a diverse population in the songbird vocal nucleus HVC. We used the completed models to predict responses to novel injected currents and cross-validated the predictions against the recorded responses to those stimuli. Using a broad range of metrics that emphasized different features of the response, we found that prediction errors were comparable to intrinsic variation in the neurons' responses, indicating that the models' behaviors closely matched those of the neurons at multiple levels of detail.

### 3.1 Model currents

We began with a simple model containing only three voltage-gated currents and found that additional sodium, calcium, and potassium currents were necessary to obtain good predictions for over 80% of the neurons. The better performance of the more complex model was not a consequence of overfitting a larger number of free parameters, because the models were cross-validated on data that were not used in fitting. With the full complement of currents, the model had 11 unmeasured state variables and 72 unknown parameters. To our knowledge, this is the largest search space explored to date for conductance-based neuron models. The data assimilation method we employ here is a significant advance because it can efficiently estimate models of a size and complexity commensurate with the biophysics of real neurons.

The better performance of the more complex model also indicates, unsurprisingly, that the dynamics of most HVC neurons depend on more than the fast sodium and potassium currents that generate action potentials. Indeed, the differences in predicted spike shapes between the simpler and more complex model were relatively small compared to other features of the response like spike rate and timing. Many of the additional currents in the complex model had relatively low maximal conductances, but were responsible for a substantial fraction of the current flux (Fig. 9) and therefore had a substantial influence on the dynamics. These currents had slower time constants, were more tonically active, and functioned in the model to modulate the cell's excitability.

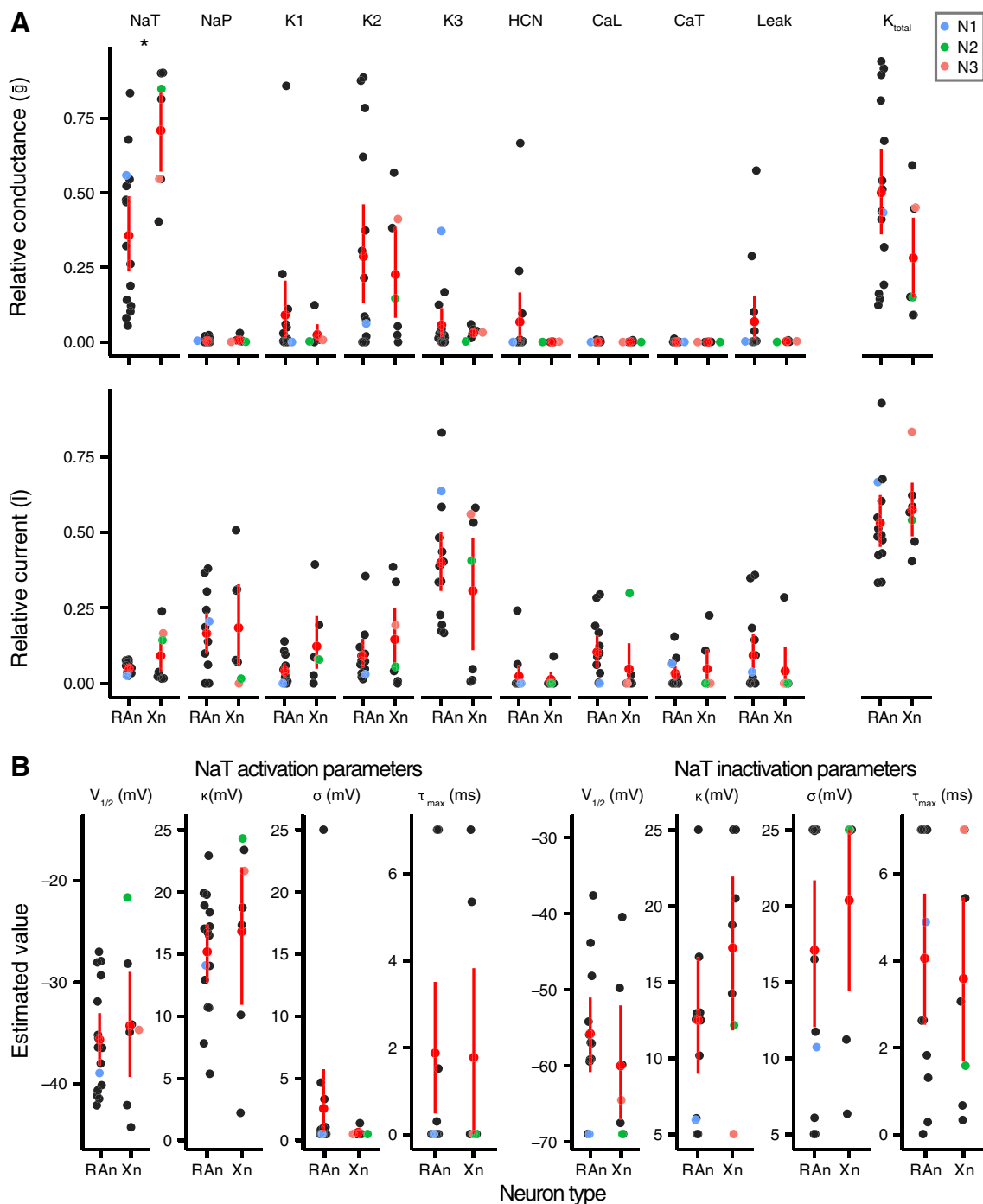


**Fig. 12** Distributions of selected parameters for 22 HVC neurons. **a** Estimated relative maximal conductances ( $\bar{g}$ , top) and relative currents ( $\bar{I}$ , bottom) for each of the currents in the model separated by the putative neuron class (RAn: projects to RA; Xn: projects to area X). Permeabilities for the calcium channels were converted to conductances by evaluating the GHK expression with the estimated calcium concentrations and  $V = 0$  mV. *Black points*, indicating individual neurons, are horizontally jittered for clarity. *Red points* and error bars indicate means and 95% confidence intervals (estimated by bootstrapping). *Light blue*,

*green*, and *red dots* correspond to exemplar neurons. *Asterisks* indicate significant difference between putative neuron classes (Wilcoxon test,  $P < 0.006$ ). Total K conductance ( $K_{total}$ ) is the sum of  $\bar{g}$  for K1–3. **b** Kinetic parameters for activation (*left*) and inactivation (*right*) of the NaT channel.  $V_{1/2}$ , half-activation;  $\kappa$ , the slope of the equilibrium state;  $\sigma$ , the width of the relaxation time function;  $\tau_{max}$ , the peak time constant. The ranges of the plot ordinates correspond to the upper and lower bounds for the parameters (color figure online)

It is important to note that we did not enforce this behavior *a priori*: The bounds for parameters governing gating time constants usually spanned several orders of magnitude (see Table S1). Instead, the slower, more modulatory nature of the additional currents emerged from the data assimilation.

Some of the currents were consistently estimated to have low maximal conductances and relative current contributions (Fig. 12), including the high-threshold calcium channel (CaL) and the hyperpolarization-activated cation channel (HCN). The data assimilation procedure effectively removed these currents from the model formulation by setting their maximal conductances close to zero. The predictions of these reduced models matched novel data, indicating that the currents do not have a strong influence on the behavior, and that the corresponding ion channels may not be expressed. On the other hand, the estimated contribution may be low because the injected currents failed to activate these channels sufficiently to affect the neuron's response. In particular, HCN is a fairly slow current and may require longer and stronger hyperpolarization than we applied in our recordings (Kubota and Taniguchi 1998; Daou et al. 2013).

The currents in the model were chosen based on a survey of the literature on HVC. The list is likely to be incomplete, and additional currents may lead to even better predictions. An attractive approach would be to include a much larger complement of currents and use maximal conductance, average current, and other methods for assessing the dynamical contribution of specific channels (e.g., Clewley 2011) to prune back to a minimal model in a systematic and controlled fashion.

### 3.2 Parameter interpretation

An important consideration in modeling studies is uncertainty in parameter estimates (Achard and Schutter 2006; Druckmann et al. 2008; Sarkar et al. 2012). Because of measurement errors, and because the model is always an approximation of the physical system, it can never perfectly reproduce the system's behavior. For a dynamical system, the distribution of parameter values that are consistent with the data is given by a high-dimensional path integral (Toth et al. 2011; Abarbanel 2013). The variational method gives a maximum likelihood estimate of the best parameters with the assumption of no model error. To incorporate model error, we sampled numerically from the path integral distribution (Kostuk et al. 2012) and found that many of the key parameters were well constrained by the data and significantly different between neurons (Fig. 10). However, most of the parameter estimates for different neurons and even different epochs from the same neuron exhibited a large degree of variance, in spite of producing similar quality predictions.

We propose several hypotheses for this variability. First, the relatively short length of the data assimilation window may mean that the current stimulation protocols insufficiently explored the state space of the model. Models estimated from different segments of data may emphasize some features of the response more than others. In support of this hypothesis, the stimulation currents we used in data assimilation did not include long step depolarizations, and in general, the models were not as good at predicting responses to step currents (Fig. 5). In further analyzing a subset of the data, we observed significantly more variability in model quality among epochs with different current protocols than among different segments of data from the same epoch. By incorporating more data with a more diverse set of injected current stimuli for assimilation, the number of solutions should shrink, although with substantially increased computational overhead.

Second, because the system is nonlinear and the model is an approximation, the parameter landscape may have many local minima. Because the variational method is based on gradient descent, it is sensitive to starting conditions and may occasionally diverge. Consistent with this hypothesis, studies with more global optimization strategies have found that most conductance-based models have multiple solutions widely separated in the parameter space (Golowasch et al. 2002; Olypher and Calabrese 2007; Achard and Schutter 2006; Druckmann et al. 2008). Expanding the model to include a larger assortment of potential currents, such as from calcium- or sodium-dependent channels (Daou et al. 2013), may ameliorate this problem by expanding the parameter space to include values closer to a true solution. Additional compartments may also allow more global minima to be found. For example, the kink observed in the phase plot of some spikes (Fig. 4) is thought to correspond to spike generation in the initial segment of the axon (Bean 2007a), where sodium channel densities are often much higher than in the soma. The model used here included only one compartment for simplicity, but as a result, the solutions represent a nonoptimal average of the two compartments.

Finally, there are likely to be degeneracies in the actual physical system such that neurons can achieve the same physiological output with different sets of parameters (Prinz and Bucher 2004; Swensen and Bean 2005; Schulz et al. 2006; Pospischil et al. 2008; Ransdell et al. 2013). The parameter variance we observed may, at least to some extent, reflect the heterogeneity of the population, even within morphologically and physiologically defined cell types. However, if this is the case, a solution for a given neuron will be only one of many it could adopt, and additional data from online pharmacological (Daou et al. 2013; Ransdell et al. 2013), dynamic clamp manipulations (Tomaiuolo et al. 2012), or network electrophysiology will be needed to constrain the solution.

### 3.3 Conclusions

Mathematical models of neural systems have the potential to reveal how details of cellular physiology and connectivity allow circuits to perform a diverse range of tasks, from extracting information from sensory inputs to generating precise patterns of motor activity. Data assimilation, the process of using observations of the voltage output of neurons to select appropriate models and infer parameter values, may serve as a useful tool toward this end. However, detailed biophysical models of real circuits have many parameters and nonlinearities, leading to complex solution spaces that may have multiple minima and present difficult optimization problems. As it is not clear what level of detail is necessary to build models that can reproduce behaviors, many recent studies have focused instead on phenomenological models, which under some conditions can provide better predictions than conductance-based models (Jolivet et al. 2004; Kobayashi et al. 2009). But it is also unclear what aspects of any one neuron's spiking response are functionally important to an animal's behavior, so the value of such comparisons is uncertain.

We have attempted to address these challenges by applying a novel method for data assimilation to neurons in HVC, a system for which the behavioral importance of precisely timed spike patterns is clear (Amador et al. 2013). We found that the method allowed us to assimilate data into models with a complement of channels sufficient to predict spike timing on par with the best phenomenological models (Jolivet et al. 2008a,b), in addition to reproducing many fine details of the neural response that the other models cannot represent.

Other methods have been developed in recent years for estimating parameters of conductance-based models, including global evolutionary algorithms (Achard and Schutter 2006; Druckmann et al. 2007) and particle filters (Huys and Paninski 2009; Vavoulis et al. 2012). One of the major advantages of the present approach is its efficiency, which supports large, complex models with many more free parameters. The ability to assimilate data to such models is a necessary step toward understanding what level of detail is needed. Further work can replace the heuristic model specification used here with a more systematic process, in which many families of channels are tested for their ability to improve spike timing predictions. Future work will also need to address questions about the role of dendritic compartments and the spatial distribution of channels in integrating inputs that do not arrive on the soma, either through calcium imaging or patch recordings from dendrites.

A significant challenge that remains is the large uncertainty in parameter estimates, as was also the case with other optimization methods when the question was addressed (Achard and Schutter 2006; Druckmann et al. 2008). In light of these uncertainties and the fact that these models are still

highly simplified relative to the neurons under study, it is premature to make strong inferences about many of the underlying biophysical properties of the neurons under study. More insight into the source of these uncertainties may be obtained by applying these methods to systems where more is known about channel types and distributions, or in which channels can be manipulated in a controlled fashion.

## 4 Materials and methods

### 4.1 Ethics statement

All animal procedures were performed according to protocols approved by the University of Chicago Institutional Animal Use and Care Committee and consistent with the guidelines of the National Institutes of Health.

### 4.2 HVC slice preparation

Slices were prepared from adult (> 90 days post hatch) male zebra finches. Birds were deeply anesthetized with isoflurane and decapitated, and the brains were placed in ice-cold, oxygenated dissection buffer containing (in mM): 205 sucrose, 3 KCl, 1 NaH<sub>2</sub>PO<sub>4</sub>, 26 NaHCO<sub>3</sub>, 25 D-glucose, 6 MgSO<sub>4</sub>, and 0.5 CaCl (290–310 mOsm). Parasagittal slices were cut (400 μm thick, Vibratome 1000) from both hemispheres and placed in 37 °C oxygenated artificial cerebrospinal fluid (ACSF) containing (in mM): 123 NaCl, 3 KCl, 1 NaH<sub>2</sub>PO<sub>4</sub>, 26 NaHCO<sub>3</sub>, 25 D-glucose, 3 MgSO<sub>4</sub>, 1 CaCl (290–310 mOsm, pH 7.2–7.3). Slices were allowed to recover for at least 1 h, during which time the ACSF was allowed to return to room temperature. For recording, slices were superfused (1.5–2.0 mL/min) with oxygenated ACSF (23–26 °C).

### 4.3 Electrophysiology

Current-clamp somatic whole-cell recordings were made from 45 neurons in HVC with an NPI SEC-05L amplifier (npi electronic, Tamm, Germany). Of these, 26 neurons had spikes with peaks > 0 mV and stable resting potential < -60 mV and were deemed suitable for analysis. Neurons were putatively classified as RA-projecting ( $n = 16$ ) if they showed strong adaptation, firing only a single spike or a short burst at the beginning of depolarization, and X-projecting ( $n = 7$ ) if they showed weak or no adaptation. One cell was classified as an interneuron based on its high firing rate and complete lack of adaptation, and two neurons could not be classified based on these criteria. Our sample is strongly biased away from interneurons because good quality recordings of these small cells are harder to achieve, and we applied stringent selection criteria to the pool of potential cells to include in

the analysis. Future studies can explore the effect of relaxing such criteria.

Cells were selected visually with differential IR optics for health but not for somatic size or shape. Patch pipettes (3–5 M $\Omega$ ) were pulled from standard-walled borosilicate glass (Model G150F-4, Warner Instruments, Hamden CT) with a Sutter P-97 (Sutter Instruments, Novato CA) and were filled with internal solution containing (in mM): 130 K-gluconate, 10 Na-gluconate, 10 HEPES, 4 NaCl, 4 MgATP, 0.3 NaGTP, 10 Na-phosphocreatine, 0.1 EGTA (290–310 mOsm, pH 7.2–7.3). In some experiments 0.50 % neurobiotin (Vector Labs, Burlingame CA) was added to the internal solution. Pipette capacitance and series resistance were compensated on the amplifier. Voltage and injected current (as reported by the amplifier) were high-pass filtered at 20 kHz and digitized at 50 kHz with a PCI-6052E (National Instruments, Austin TX). Injected currents consisted of positive and negative steps of varying amplitude and a complex, nonsinusoidal waveform derived from the Lorenz equations (e.g., Fig. 1a) delivered at varying frequencies. Previous work with simulated data indicated that white noise does not lead to good data assimilation because it fails to depolarize or hyperpolarize neurons for enough time to sufficiently activate some kinds of channels (Toth et al. 2011). The amplitude of the complex current was adjusted online to ensure that spikes were elicited and the neuron was hyperpolarized to at least -90 mV for some period of time. Data collection was controlled by custom software written in MATLAB (The Mathworks, Natick MA).

#### 4.4 Dynamical state and parameter estimation of neuron models

Data assimilation is the general name given to the incorporation of information from measurements of a physical system into a set of model dynamical equations with the goal of finding a set of parameters and state variables such that the model best describes the data. We call a model with parameters estimated in this manner a completed model. In this preparation, the data to be assimilated were the measurements of membrane potential from the somatic current-clamp electrode, which was also used to deliver selected forcing by current injection. The same principles apply to preparations in which data from other parts of the cell are available from other electrodes or fluorescent reporters (Jin et al. 2012).

Statistical properties of estimated quantities, such as the expected state during a learning window, or in a prediction window following the learning period, along with the estimated errors of these expected values, are given by the evaluation of a path integral through the state space of the model (Jouvet and Phythian 1979; Hochberg et al. 1999; Restrepo 2008; Abarbanel 2009). The appropriate integrals can be approximated numerically using Monte Carlo sampling techniques (Kostuk et al. 2012). Here, we used a combined

approach in which parameter estimates were first obtained by a variational method that approximates these integrals using a saddle point approach to minimize an objective function, providing the maximum likelihood estimate of the distribution. These estimates were then used as starting values in a Monte Carlo algorithm to sample from the full path integral distribution (see Sect. 4.6). As with all optimization methods, the variational approach has strengths and weaknesses (Wolpert and Macready 1997), but it remains a reliable choice for deterministic systems where the derivatives are available (Gill et al. 1981; Wächter 2002). One benefit is that the optimization of state variables, including the data dimension, is performed at every time point. This allows for a generic choice of objective function measure, such as least-squares used here (Eq. 1), avoiding the question of how to incorporate more subjective measures such as spike number, rise-times, and inter-spike-interval into a meaningful objective function.

A critical concern in variational approaches to nonlinear dynamical systems is that the familiar least-squares objective function may give an irregular search surface with many local minima (Abarbanel et al. 2010). We addressed this problem by including a balanced synchronization term,  $u(t)(V_{\text{data}}(t) - V_m(t))$ , in the model dynamics, which regularizes and minimizes the influence of local minima by ensuring that the solution set defines a model that is capable of synchronizing with the data (Huijberts et al. 2001; Abarbanel et al. 2008, 2009; Szendro et al. 2009). The objective function has a penalty for this regularization and is taken as

$$\frac{1}{T} \sum_{t=1}^T \left\{ (V_{\text{data}}(t) - V_m(t))^2 + u(t)^2 \right\}, \quad (1)$$

where  $V_{\text{data}}(t)$  is the measured voltage,  $V_m(t)$  is the voltage output from the model, and  $T$  is the number of discretely sampled time points.

The neuron model that we investigated is not known to be chaotic for the biophysical range of our parameters, but it is nonlinear, and in the high-dimensional search space, there may well exist chaotic regions that must be explored by the optimization routine, and these will benefit from this regularization. We have shown using simulated data that the variational approach using this regularized cost function can recover unmeasured states and parameters, including both maximal conductances and channel kinetics (Abarbanel et al. 2011; Toth et al. 2011). Example data and code for data assimilation are available in online supplemental material.

Provided a solution to the model can be found that is consistent with the data, at the end of the optimization, the value for the control parameter  $u(t)$ , governing the magnitude of the synchronization term, should be small relative to the model dynamics. The quality of the model was tested by setting  $u(t)$  to zero and integrating the model forward

from the end of the assimilation period using the estimated parameter and state values. The integration algorithm was fourth-order Runge–Kutta with timestep 0.02 ms.

#### 4.5 Model validation

The intra-epoch predictions for completed models were compared to recorded data using five metrics, which have been used in other studies of neural models and which represent complementary aspects of the neural response. The correlation coefficient (CC) was the simplest metric, and the most closely related to the objective function used to fit the model. We note that CC strongly penalizes errors in spike timing greater than the width of a spike. The other four metrics required separating the spikes from the subthreshold voltage. Spikes were detected by an algorithm that determined when the voltage crossed a threshold and then located the next peak within 1.5 ms of the threshold crossing. The time of the peak was considered the spike time. For each spike, the voltage values between 3.5 ms before the peak and 8.0 ms after were extracted to give the spike waveform. The subthreshold voltage was defined by clipping out time points contiguous with the peak of the spike where  $V(t) > -50$  mV.

Subthreshold voltage deviance was calculated as the RMS difference between time points in the predicted and measured voltage, excluding points that had been clipped out around spikes in either time series. Larger values indicate worse predictions.

Spike rate deviance was calculated as  $|N_p - N_m| / \max(N_p, N_m)$ , where  $N_p$  was the number of predicted spikes and  $N_m$  the number of measured spikes. The value of this metric is bounded between 0 and 1, with larger values indicating greater errors in the predicted spike rate.

Spike shape deviance was calculated by creating a 2-D histogram of the spike waveforms in the phase plane (as in Fig. 1e), with one axis corresponding to  $V(t)$  and the other to  $dV(t)/dt$  (Druckmann et al. 2007). Histograms were bounded between  $-90$  to  $60$  mV, and  $-1,000$  to  $1,500$  mV/ms, with 100 bins in each dimension. The histograms were normalized to a total area of 1.0, and the deviance was the RMS difference between the histograms. This metric accounts for variation in spike waveform, so that if spikes change shape (in a burst, for example) in the data but not the model, the deviance will increase. Values are bounded between 0 and 1, with larger values indicating larger errors.

Spike timing, which is likely to be the most important feature of the response in terms of function in singing, was compared using the coincidence factor  $\Gamma$  (Jolivet et al. 2008b), with a window size of 2 ms. This metric has been widely used in modeling studies (Jolivet et al. 2008b) and has the advantage of not being strongly dependent on the duration of the coincidence window. It compares the number of coincident

spikes observed between data and prediction with the number of coincidences expected from a homogeneous Poisson process with the same rate. Scores indicate the proportion of predictable spikes actually predicted by the model.

When possible, the prediction metrics were also calculated between the assimilation epoch and another epoch with the same stimulus, as a measure of the neurons’ intrinsic variability. Not enough neurons were presented with the same stimuli multiple times to enable scores for individual neurons to be corrected for intrinsic variability, so we pooled estimates across the population. There was a trend for putative RA-projecting neurons to be more reliable ( $\Gamma = 0.56 \pm 0.06$ ) than X-projecting neurons ( $\Gamma = 0.30 \pm 0.08$ ), but the difference was not statistically significant ( $t$  test,  $P = 0.08$ ).

To choose the best overall model for each neuron, scores on each of the metrics were ranked, with a rank of 1 indicating the lowest deviance, highest correlation, or highest coincidence. Ranks were summed across metrics, and the model with the lowest sum was considered the best overall. CC was used to break ties.

#### 4.6 Parameter uncertainty calculations

The uncertainty in a solution is dependent upon both measurement and model error and is expressed by the joint probability distribution resulting from the path integral defined in Toth et al. (2011). This integral can be approximated with numerical sampling, as discussed in detail in Kostuk et al. (2012). Both measurement and model error were approximated as Gaussian, with measurement error  $\sigma_m = 0.4$  mV (obtained experimentally) and model error  $\sigma_f = 0.04$  (mV for  $V_m$ , unitless for the gating particles). Using this approximation, we sampled the path distribution

$$P(\mathbf{y}(t) | V_{\text{data}}(t)) \propto e^{-A_0(\mathbf{y}(t), V_{\text{data}}(t))},$$

with the action,  $A_0$ , given by

$$A_0 = \frac{1}{2T\sigma_m^2} \sum_{t=0}^T (y_1(t) - V_{\text{data}}(t))^2 + \frac{1}{2T\sigma_f^2} \sum_{t=0}^{T-1} \sum_{i=1}^{12} \text{TRP}^2(y_i(t), y_i(t+1)), \quad (2)$$

using Metropolis-Hastings Monte Carlo (Metropolis et al. 1953; Hastings 1970). Briefly, the Metropolis-Hastings method is an iterative algorithm with the following steps. First, values for the states and parameters from the previous iteration are randomly altered. Second, the action (Eq. 2) is calculated for the new parameter values and compared to the action in the previous step. Third, if the action decreases, the new parameter values are accepted; if the action increases,

the new parameter values are accepted with a probability proportional to the action.

The model errors are represented in the TRP function, which is the error of the trapezoidal integration rule between the model values at time  $t$  and  $t + 1$ . The objective function (Eq. 1) used for the variational optimization is clearly reminiscent of the action (Eq. 2) but in the limit of vanishing model error where instead the model equations are enforced as constraints. The solution of the variational optimization obtains  $u(t) \approx 0$  and represents the maximum likelihood path of this distribution.

To calculate parameter uncertainty, the time series of model variables was down-sampled from 50 to 5 kHz, although the entire data assimilation window was used. The initial path was provided by the result of the variational optimization, and the chain was allowed to explore the space about this solution while accepting 5 % increases in the objective function with 50 % probability. A random perturbation to all variables,  $(\mathbf{y}(t), p)$  was considered one step in the Markov chain. The chain was allowed to come to equilibrium over  $5 \times 10^6$  steps, and then,  $1 \times 10^3$  samples were taken, uniformly distributed over the next  $2 \times 10^6$  steps.

#### 4.7 Neuron model

We used a single-compartment, isopotential model with a passive leak conductance and eight active, voltage-gated conductances. We developed the model iteratively, starting with the standard Hodgkin–Huxley transient sodium and noninactivating potassium channels, along with a nonselective hyperpolarization-activated cation channel (HCN). This model was used in an earlier study with simulated data (Toth et al. 2011), which showed that the variational method could recover the states and parameters of the model used to simulate data. However, we found that this simple model was unable to reproduce several features of our recordings from real neurons in HVC, so we added additional sodium, potassium, and calcium channels that have been found in a broad range of neurons, some in HVC (Kubota and Saito 1991). In the absence of data on the expression patterns of specific ion channel genes in HVC, we chose relatively wide parameter bounds for the channel kinetic parameters, thereby allowing the currents to represent classes of channels with similar voltage dependence and gating kinetics. The membrane voltage  $V_m$  is given by the current conservation equation

$$\frac{dV_m(t)}{dt} = \frac{1}{C_m} (I_{\text{NaT}} + I_{\text{NaP}} + I_{K1} + I_{K2} + I_{K3} + I_{\text{HCN}} + I_{\text{CaL}} + I_{\text{CaT}} + I_{\text{Leak}} + I_{\text{inj}}/I_{\text{SA}}), \quad (3)$$

where  $C_m$  is the specific membrane capacitance, and  $I_{\text{SA}}$  is a parameter relating to the surface area of the membrane; it sets the scale of the injected current actually seen by the neuron. The  $I_X$  are channel currents. Each of the voltage-gated currents depends on ion flow through channels whose permeability is controlled by activation ( $m$ ) and inactivation ( $h$ ) gating variables.  $I_{\text{ion}}(t) = g_{\text{ion}} m(t)^{n1} h(t)^{n2} (E_{\text{reversal}} - V_m(t))$ , where  $g_{\text{ion}}$  is a maximal conductance and  $n1, n2$  are integers. The voltage-gated currents we included are transient sodium ( $I_{\text{NaT}}$ ; kinetics  $m^3h$ ), persistent sodium ( $I_{\text{NaP}}$ ;  $m$ ), noninactivating fast potassium ( $I_{K1}$ ;  $m^4$ ), inactivating potassium ( $I_{K2}$ ;  $m^4h$ ), slow potassium ( $I_{K3}$ ;  $m$ ), hyperpolarization-activated cation ( $I_{\text{HCN}}$ ;  $h$ ), high-threshold L-type calcium ( $I_{\text{CaL}}$ ;  $m^2h$ ), and low-threshold T-type calcium ( $I_{\text{CaT}}$ ;  $m^2$ ).

Each of the sodium, potassium, and leak currents was modeled by the Nernst approximation to the Goldman–Hodgkin–Katz (GHK) current equation,  $I_\alpha = g_\alpha X_\alpha (E_{\text{rev}} - V_m)$ , where  $g_\alpha$  is the maximal conductance of the channel,  $X_\alpha$  is a channel-dependent and voltage-dependent function related to the proportion of open channels, and  $E_{\text{rev}}$  is the reversal potential of the active ion species. Due to the large differences in intra- and extracellular calcium concentrations, the full GHK equation was used to describe these currents. For numerical stability, we used a 24th-order polynomial expansion of this equation.

The permeability of each voltage-gated channel species depended on one or more gating variables (e.g.,  $m, h$ ) whose opening and closing were modeled by the Boltzmann barrier-hopping rate,

$$\frac{dm(t)}{dt} = \frac{m_\infty(V_m(t)) - m(t)}{\tau(V_m(t))}, \quad (4)$$

where  $m_\infty(V)$  gives the equilibrium activation and  $\tau(V)$  gives the time constant as functions of voltage. In terms of the opening rate  $\alpha(V)$  and closing rate  $\beta(V)$  in the original Hodgkin–Huxley formulation (Hodgkin and Huxley 1952),  $m_\infty = \alpha/(\alpha + \beta)$  and  $\tau = 1/(\alpha + \beta)$ . These functions are usually expressed in terms of exponentials, but for numerical stability, we used a hyperbolic tangent approximation, with

$$m_\infty(V_m) = 0.5(1 + \tanh((V_m(t) - V_{1/2})/\kappa)), \\ \tau(V_m) = \tau_0 + \tau_{\text{max}}(1 - \tanh^2((V_m(t) - V_{1/2})/\sigma)). \quad (5)$$

In this representation,  $V_{1/2}$  is the half-activation voltage,  $\kappa$  is the slope of the activation function between the closed and open state,  $\tau_0$  is the minimum relaxation time,  $\tau_{\text{max}} + \tau_0$  is the peak relaxation time, and  $\sigma$  is the width of the relaxation time function. Equations for the inactivation variables ( $h$ ) have a similar form (see Table 3). For the K2 and CaT inactivation particles, we used a more complex form that allowed

**Table 3** Full set of differential equations for the conductance-based neuron model

---

**Voltage** :  $dy_1/dt = ((p_2y_2^3y_3 + p_3y_4)(p_4 - y_1) + (p_5y_5^4 + p_6y_6^4y_7 + p_7y_8)(p_8 - y_1) + (p_7y_9^2 + p_72y_{10}^2y_{11})19.2970673(p_{11} - 0.0001 \exp(y_1/13))/\text{GHK}(y_1) + p_9(p_{10} - y_1) + p_{12}y_{12}(-43 - y_1) + I_{inj}/p_{13})/p_1 + u(t)(V_{data}(t) - y_1)$

**NaT, m** :  $dy_2/dt = 0.5(1 + \tanh((y_1 - p_{14})/p_{15}) - 2y_2)/(p_{17} + p_{18}(1 - \tanh^2((y_1 - p_{14})/p_{16})))$

**NaT, h** :  $dy_3/dt = 0.5(1 + \tanh((y_1 - p_{19})/p_{20}) - 2y_3)/(p_{22} + p_{23}(1 - \tanh^2((y_1 - p_{19})/p_{21})))$

**NaP, m** :  $dy_4/dt = 0.5(1 + \tanh((y_1 - p_{24})/p_{25}) - 2y_4)/(p_{27} + p_{28}(1 - \tanh^2((y_1 - p_{24})/p_{26})))$

**K1, m** :  $dy_5/dt = 0.5(1 + \tanh((y_1 - p_{29})/p_{30}) - 2y_5)/(p_{32} + p_{33}(1 - \tanh^2((y_1 - p_{29})/p_{31})))$

**K2, m** :  $dy_6/dt = 0.5(1 + \tanh((y_1 - p_{34})/p_{35}) - 2y_6)/(p_{37} + p_{38}(1 - \tanh^2((y_1 - p_{34})/p_{36})))$

**K2, h** :  $dy_7/dt = 0.5(1 + \tanh((y_1 - p_{39})/p_{40}) - 2y_7)/(p_{42} + p_{44} + 0.5(1 - \tanh(y_1 - p_{39})) \cdot (p_{43}(1 - \tanh^2((y_1 - p_{39})/p_{41})) - p_{44}))$

**K3, m** :  $dy_8/dt = 0.5(1 + \tanh((y_1 - p_{45})/p_{46}) - 2y_8)/(p_{48} + p_{49}(1 - \tanh^2((y_1 - p_{45})/p_{47})))$

**CaT, m** :  $dy_9/dt = 0.5(1 + \tanh((y_1 - p_{50})/p_{51}) - 2y_9)/(p_{53} + p_{54}(1 - \tanh^2((y_1 - p_{50})/p_{52})))$

**CaL, m** :  $dy_{10}/dt = 0.5(1 + \tanh((y_1 - p_{55})/p_{56}) - 2y_{10})/(p_{58} + p_{59}(1 - \tanh^2((y_1 - p_{55})/p_{57})))$

**CaL, h** :  $dy_{11}/dt = 0.5(1 + \tanh((y_1 - p_{60})/p_{61}) - 2y_{11})/(p_{64} + p_{65}(1 + \tanh((y_1 - p_{60})/p_{62})) \cdot (1 - \tanh((y_1 - p_{60})/p_{63}))(1 - \tanh(y_1 - p_{60}) \tanh((1/p_{62} + 1/p_{63})(y_1 - p_{60}))) / (1 + \tanh((y_1 - p_{60})/p_{62}) \tanh((y_1 - p_{60})/p_{63})))$

**HCN, h** :  $dy_{12}/dt = 0.5(1 + \tanh((y_1 - p_{66})/p_{67}) - 2y_{12})/(p_{69} + p_{70}(1 - \tanh^2((y_1 - p_{66})/p_{68})))$

---

relaxation voltage dependence to be asymmetric (see Table 3 below).

The membrane voltage and the values for the gating variables formed a 12-dimensional vector  $\{y_1(t), y_2(t), \dots, y_{12}(t)\}$  that described the state of the neuron. The dynamics of the state vector were defined by a set of ordinary differential equations that depended on a number of unknown parameters. The complete set of model equations used for the optimization procedure, including the synchronization-inspired regularization term, are given in Table 3.

#### 4.8 Numerical analysis details

Optimization was accomplished using the interior-point algorithm provided by the open source software IPOPT (Wächter 2002) and the pardiso (Schenk et al. 2008) or ma57 linear solver libraries, on standard desktop hardware and on a Cray XE6. The data assimilation window over which the model properties were estimated was 1,500 ms long; the data were sampled at 50 kHz, resulting in 75,000 time points of voltage data. Common to ‘direct method’ variational approaches, the model trajectories were co-located during the optimization procedure; that is, each component of  $\{y_1(t), y_2(t), \dots, y_{12}(t)\}$  was treated as an independent variable with the model dynamical equations imposed as equality constraints between neighboring time points. Gating particle variables were constrained between 0 and 1, and each of the parameters was constrained between biologically realistic bounds (see Table S1). Data assimilation of the full model

took an average of 52 h (range 14–199 h) of computation per epoch on a single core.

The completed model, with estimated parameters and state variables at  $t = 1,500$  ms, was then integrated forward with  $u(t) = 0$  for the remainder of the data epoch with the same injected current that was presented to the real neuron. To generate predictions on different data epochs, a short (100 ms) section of data was used to find the initial conditions for the state variables (the parameters being held fixed at their previously established values), and then, the model was integrated forward again with the corresponding injected current and  $u(t) = 0$ .

As a technical note, it is essential to fully exercise the range of the neuron’s dynamics during the data assimilation window (Hobbs and Hooper 2008). This is achieved by subjecting the neuron to a current with a complicated waveform, exhibiting a broad power spectrum (many characteristic timescales) as well as regions of constant (positive, negative, and zero) current to ascertain the neuron’s passive response properties. High frequency currents are not useful as they are filtered out by the RC time constant of the membrane. Our results also indicate that long-duration, low-frequency currents (including steps) may be essential for uncovering slow potentials like the HCN current. More naturalistic currents may fail to uncover contributions from channels with slower kinetics or smaller maximal conductances or may require much longer assimilation windows for those contributions to have a significant influence on the estimated parameters.

**Acknowledgments** B. Toth contributed software used to generate IPOPT code. We acknowledge many productive conversations with P. E. Gill on numerical optimization, and we thank A. Daou for conversations about neuron classes in HVC. Support from the US Department of Energy (Grant DE-SC0002349) and the National Science Foundation (Grants IOS-0905076, IOS-0905030, and PHY-0961153) is gratefully acknowledged. Partial support from the NSF sponsored Center for Theoretical Biological Physics is also appreciated.

## References

- Abarbanel HDI (2009) Effective actions for statistical data assimilation. *Phys Lett A* 373:4044–4048
- Abarbanel HDI (2013) Predicting the future: completing models of complex systems. Springer, New York
- Abarbanel HDI, Creveling D, Jeanne J (2008) Estimation of parameters in nonlinear systems using balanced synchronization. *Phys Rev E* 77(016):208
- Abarbanel HDI, Creveling DR, Farsian R, Kostuk M (2009) Dynamical state and parameter estimation. *SIAM J Appl Dyn Syst* 8(4):1341–1381
- Abarbanel HDI, Kostuk M, Whartenby W (2010) Data assimilation with regularized nonlinear instabilities. *Q J Meteor Soc* 136(648):769–783
- Abarbanel HDI, Bryant P, Gill PE, Kostuk M, Rofeh J, Singer Z, Toth B, Wong E (2011) Dynamical parameter and state estimation in neuron models. In: Glanzman D, Ding M (eds) *The dynamic brain: an exploration of neuronal variability and its functional significance*, chap 8. Oxford University Press, New York
- Achard P, Schutter ED (2006) Complex parameter landscape for a complex neuron model. *PLoS Comput Biol* 2(7):e94. doi:10.1371/journal.pcbi.0020094
- Amador A, Perl YS, Mindlin GB, Margoliash D (2013) Elemental gesture dynamics are encoded by song premotor cortical neurons. *Nature* 495(7439):59–64. doi:10.1038/nature11967
- Ayali A, Lange AB (2010) Rhythmic behaviour and pattern-generating circuits in the locust: key concepts and recent updates. *J Insect Physiol* 56(8):834–843. doi:10.1016/j.jinsphys.2010.03.015
- Baldi P, Vanier MC, Bower JM (1998) On the use of Bayesian methods for evaluating compartmental neural models. *J Comput Neurosci* 5:285–314
- Bean BP (2007a) The action potential in mammalian central neurons. *Nat Rev Neurosci* 8(6):451–465. doi:10.1038/nrn2148
- Bean BP (2007b) The action potential in mammalian central neurons. *Nat Rev Neurosci* 8(6):451–465. doi:10.1038/nrn2148
- Briggman KL, Abarbanel HDI, Kristan WB (2005) Optical imaging of neuronal populations during decision-making. *Science* 307:896–901
- Buhry L, Pace M, Saighi S (2012) Global parameter estimation of an Hodgkin–Huxley formalism using membrane voltage recordings: application to neuro-mimetic analog integrated circuits. *Neurocomputing* 81:75–85. doi:10.1016/j.neucom.2011.11.002
- Cerda O, Trimmer JS (2010) Analysis and functional implications of phosphorylation of neuronal voltage-gated potassium channels. *Neurosci Lett* 486(2):60–7. doi:10.1016/j.neulet.2010.06.064
- Clewley R (2011) Inferring and quantifying the role of an intrinsic current in a mechanism for a half-center bursting oscillation: a dominant scale and hybrid dynamical systems analysis. *J Biol Phys* 37(3):285–306
- Daou A, Ross M, Johnson F, Hyson RL, Bertram R (2013) Electrophysiological characterization and computational models of HVC neurons in the zebra finch. *J Neurophysiol*. doi:10.1152/jn.00162.2013
- Druckmann S, Banitt Y, Gidon A, Schürmann F, Markram H, Segev I (2007) A novel multiple objective optimization framework for constraining conductance-based neuron models by experimental data. *Front Neurosci* 1(1):7–18. doi:10.3389/neuro.01.1.1.001.2007
- Druckmann S, Berger TK, Hill S, Schürmann F, Markram H, Segev I (2008) Evaluating automated parameter constraining procedures of neuron models by experimental and surrogate data. *Biol Cybern* 99(4–5):371–9. doi:10.1007/s00422-008-0269-2
- Dutar P, Vu HM, Perkel DJ (1998) Multiple cell types distinguished by physiological, pharmacological, and anatomic properties in nucleus HVC of the adult zebra finch. *J Neurophysiol* 80(4):1828–1838
- Fortune ES, Margoliash D (1995) Parallel pathways and convergence onto HVC and adjacent neostriatum of adult zebra finches (*Taeniopygia guttata*). *J Comp Neurol* 360(3):413–441. doi:10.1002/cne.903600305
- Foster WR, Ungar LH, Schwaber JS (1993) Significance of conductances in Hodgkin–Huxley models. *J Neurophysiol* 70(6):2502–2518
- Geit WV, Schutter ED, Achard P (2008) Automated neuron model optimization techniques: a review. *Biol Cybern* 99:241–251. doi:10.1007/s00422-008-0257-6
- Gill PE, Murray W, Wright MH (1981) *Practical optimization*. Academic Press, London
- Gleeson P, Crook S, Cannon RC, Hines ML, Billings GO, Farinella M, Morse TM, Davison AP, Ray S, Bhalla US, Barnes SR, Dimitrova YD, Silver RA (2010) NeuroML: a language for describing data driven models of neurons and networks with a high degree of biological detail. *PLoS Comput Biol* 6(6):e1000815. doi:10.1371/journal.pcbi.1000815
- Golowasch J, Goldman MS, Abbott LF, Marder E (2002) Failure of averaging in the construction of a conductance-based neuron model. *J Neurophysiol* 87(2):1129–31
- Günay C, Edgerton JR, Jaeger D (2008) Channel density distributions explain spiking variability in the globus pallidus: a combined physiology and computer simulation database approach. *J Neurosci* 28(30):7476–7491. doi:10.1523/JNEUROSCI.4198-07.2008
- Hahnloser RHR, Kozhevnikov AA, Fee MS (2002) An ultra-sparse code underlies the generation of neural sequences in a songbird. *Nature* 419:65–70
- Hastings WK (1970) Monte Carlo sampling methods using Markov chains and their applications. *Biometrika* 57(1):97
- Hendrickson EB, Edgerton JR, Jaeger D (2011) The use of automated parameter searches to improve ion channel kinetics for neural modeling. *J Comput Neurosci* 31(2):329–346. doi:10.1007/s10827-010-0312-x
- Herz AVM, Gollisch T, Machens CK, Jaeger D (2006) Modeling single-neuron dynamics and computations: a balance of detail and abstraction. *Science* 314(5796):80–85. doi:10.1126/science.1127240
- Hines ML, Carnevale NT (1997) The NEURON simulation environment. *Neural Comput* 9(6):1179–1209
- Hobbs KH, Hooper SL (2008) Using complicated, wide dynamic range driving to develop models of single neurons in single recording sessions. *J Neurophysiol* 99(4):1871–83. doi:10.1152/jn.00032.2008
- Hochberg D, Molina-París C, Pérez-Mercader J, Visser M (1999) Effective action of stochastic partial differential equations. *Phys Rev E* 60(6):6343–6360
- Hodgkin AL, Huxley AF (1952) A quantitative description of membrane current and its application to conduction and excitation in nerve. *J Physiol (Lond)* 117(4):500–44
- Huijberts HJC, Lilge T, Nijmeijer H (2001) Nonlinear discrete-time synchronization via extended observers. *Int J Bifurcat Chaos* 11(7):1997–2006
- Huys QJM, Paninski L (2009) Smoothing of, and parameter estimation from, noisy biophysical recordings. *PLoS Comput Biol* 5(5):e1000379. doi:10.1371/journal.pcbi.1000379

- Huys QJM, Ahrens MB, Paninski L (2006) Efficient estimation of detailed single-neuron models. *J Neurophysiol* 96(2):872–90. doi:[10.1152/jn.00079.2006](https://doi.org/10.1152/jn.00079.2006)
- Jin D, Ramazanoğlu F, Seung H (2007) Intrinsic bursting enhances the robustness of a neural network model of sequence generation by avian brain area HVC. *J Comput Neurosci* 23(3):283–299
- Jin L, Han Z, Platisa J, Wooltorton JR, Cohen LB, Pieribone VA (2012) Single action potentials and subthreshold electrical events imaged in neurons with a fluorescent protein voltage probe. *Neuron* 75(5):779–785. doi:[10.1016/j.neuron.2012.06.040](https://doi.org/10.1016/j.neuron.2012.06.040)
- Johnston J, Forsythe ID, Kopp-Scheinflug C (2010) Going native: voltage-gated potassium channels controlling neuronal excitability. *J Physiol (Lond)* 588(Pt 17):3187–3200. doi:[10.1113/jphysiol.2010.191973](https://doi.org/10.1113/jphysiol.2010.191973)
- Jolivet R, Lewis TJ, Gerstner W (2004) Generalized integrate-and-fire models of neuronal activity approximate spike trains of a detailed model to a high degree of accuracy. *J Neurophysiol* 92(2):959–76. doi:[10.1152/jn.00190.2004](https://doi.org/10.1152/jn.00190.2004)
- Jolivet R, Kobayashi R, Rauch A, Naud R, Shinomoto S, Gerstner W (2008a) A benchmark test for a quantitative assessment of simple neuron models. *J Neurosci Methods* 169(2):417–424. doi:[10.1016/j.jneumeth.2007.11.006](https://doi.org/10.1016/j.jneumeth.2007.11.006)
- Jolivet R, Schürmann F, Berger TK, Naud R, Gerstner W, Roth A (2008b) The quantitative single-neuron modeling competition. *Biol Cybern* 99(4–5):417–426. doi:[10.1007/s00422-008-0261-x](https://doi.org/10.1007/s00422-008-0261-x)
- Jouvet B, Phythian R (1979) Quantum aspects of classical and statistical fields. *Phys Rev A* 19(3):1350–1355
- Kew JNC, Davies CH (eds) (2010) Ion channels: from structure to function. Oxford University Press, New York
- Kobayashi R, Tsubo Y, Shinomoto S (2009) Made-to-order spiking neuron model equipped with a multi-timescale adaptive threshold. *Front Comput Neurosci* 3:9. doi:[10.3389/neuro.10.009.2009](https://doi.org/10.3389/neuro.10.009.2009)
- Kole MH, Hallermann S, Stuart GJ (2006) Single Ih channels in pyramidal neuron dendrites: properties, distribution, and impact on action potential output. *J Neurosci* 26(6):1677–1687. doi:[10.1523/JNEUROSCI.3664-05.2006](https://doi.org/10.1523/JNEUROSCI.3664-05.2006)
- Kostuk M, Toth BA, Meliza CD, Margoliash D, Abarbanel HDI (2012) Dynamical estimation of neuron and network properties II: path integral monte carlo methods. *Biol Cybern* 106(3):155–167. doi:[10.1007/s00422-012-0487-5](https://doi.org/10.1007/s00422-012-0487-5)
- Kubota M, Saito N (1991) Sodium- and calcium-dependent conductances of neurones in the zebra finch hyperstriatum ventrale pars caudale in vitro. *J Physiol (Lond)* 440:131–142
- Kubota M, Taniguchi I (1998) Electrophysiological characteristics of classes of neuron in the HVC of the zebra finch. *J Neurophysiol* 80(2):914–923
- Lepora NF, Overton PG, Gurney K (2011) Efficient fitting of conductance-based model neurons from somatic current clamp. *J Comput Neurosci*. doi:[10.1007/s10827-011-0331-2](https://doi.org/10.1007/s10827-011-0331-2)
- Long MA, Jin DZ, Fee MS (2010) Support for a synaptic chain model of neuronal sequence generation. *Nature* 468(7322):394–9. doi:[10.1038/nature09514](https://doi.org/10.1038/nature09514)
- Marder E, Bucher D (2007) Understanding circuit dynamics using the stomatogastric nervous system of lobsters and crabs. *Annu Rev Physiol* 69:291–316. doi:[10.1146/annurev.physiol.69.031905.161516](https://doi.org/10.1146/annurev.physiol.69.031905.161516)
- Metropolis N, Rosenbluth AW, Rosenbluth MN, Teller AH, Teller E (1953) Equation of state calculations by fast computing machines. *J Chem Phys* 21(6):1087–1092
- Mooney R (2000) Different subthreshold mechanisms underlie song selectivity in identified HVC neurons of the zebra finch. *J Neurosci* 20(14):5420–5436
- Mooney R, Prather JF (2005) The HVC microcircuit: the synaptic basis for interactions between song motor and vocal plasticity pathways. *J Neurosci* 25(8):1952–1964. doi:[10.1523/JNEUROSCI.3726-04.2005](https://doi.org/10.1523/JNEUROSCI.3726-04.2005)
- Nixdorf B, Davis S, DeVoogd T (1989) Morphology of Golgi-impregnated neurons in hyperstriatum ventralis, pars caudalis in adult male and female canaries. *J Comp Neurol* 284(3):337–349. doi:[10.1002/cne.902840302](https://doi.org/10.1002/cne.902840302)
- Olypher AV, Calabrese RL (2007) Using constraints on neuronal activity to reveal compensatory changes in neuronal parameters. *J Neurophysiol* 98(6):3749–58. doi:[10.1152/jn.00842.2007](https://doi.org/10.1152/jn.00842.2007)
- Pospischil M, Toledo-Rodriguez M, Monier C, Piwkowska Z, Bal T, Frégnac Y, Markram H, Destexhe A (2008) Minimal Hodgkin–Huxley type models for different classes of cortical and thalamic neurons. *Biol Cybern* 99(4–5):427–441. doi:[10.1007/s00422-008-0263-8](https://doi.org/10.1007/s00422-008-0263-8)
- Prinz AA, Billimoria CP, Marder E (2003) Alternative to hand-tuning conductance-based models: construction and analysis of databases of model neurons. *J Neurophysiol* 90(6):3998–4015. doi:[10.1152/jn.00641.2003](https://doi.org/10.1152/jn.00641.2003)
- Prinz AA, Bucher DEM (2004) Similar network activity from disparate circuit parameters. *Nat Neurosci* 7:1345–1352
- Ransdell J, Nair S, Schulz D (2013) Neurons within the same network independently achieve conserved output by differentially balancing variable conductance magnitudes. *J Neurosci* 33(24):9950–9956. doi:[10.1523/JNEUROSCI.1095-13.2013](https://doi.org/10.1523/JNEUROSCI.1095-13.2013)
- Reid MS, Brown EA, DeWeerth SP (2007) A parameter-space search algorithm tested on a Hodgkin–Huxley model. *Biol Cybern* 96(6):625–634. doi:[10.1007/s00422-007-0156-2](https://doi.org/10.1007/s00422-007-0156-2)
- Restrepo JM (2008) A path integral method for data assimilation. *Physica D* 237:14–27
- Roberts TF, Klein ME, Kubke MF, Wild JM, Mooney R (2008) Telencephalic neurons monosynaptically link brainstem and forebrain premotor networks necessary for song. *J Neurosci* 28(13):3479–3489. doi:[10.1523/JNEUROSCI.0177-08.2008](https://doi.org/10.1523/JNEUROSCI.0177-08.2008)
- Sarkar AX, Christini DJ, Sobie EA (2012) Exploiting mathematical models to illuminate electrophysiological variability between individuals. *J Physiol (Lond)* 590(Pt 11):2555–67. doi:[10.1113/jphysiol.2011.223313](https://doi.org/10.1113/jphysiol.2011.223313)
- Schenk O, Bollhoefer M, Gärtner K (2008) On large-scale diagonalization techniques for the Anderson model of localization. *SIAM Rev* 50:91–112
- Schulz DJ, Gaouillard JM, Marder E (2006) Variable channel expression in identified single and electrically coupled neurons in different animals. *Nat Neurosci* 9(3):356–362. doi:[10.1038/nn1639](https://doi.org/10.1038/nn1639)
- Shea SD, Koch H, Baleckaitis D, Ramirez JM, Margoliash D (2010) Neuron-specific cholinergic modulation of a forebrain song control nucleus. *J Neurophysiol* 103(2):733–745. doi:[10.1152/jn.00803.2009](https://doi.org/10.1152/jn.00803.2009)
- Swensen AM, Bean BP (2005) Robustness of burst firing in dissociated Purkinje neurons with acute or long-term reductions in sodium conductance. *J Neurosci* 25(14):3509–20. doi:[10.1523/JNEUROSCI.3929-04.2005](https://doi.org/10.1523/JNEUROSCI.3929-04.2005)
- Szendro IG, Rodríguez MA, López JM (2009) On the problem of data assimilation by means of synchronization. *J Geophys Res*. doi:[10.1029/2009JD012411](https://doi.org/10.1029/2009JD012411)
- Tomaiuolo M, Bertram R, Leng G, Tabak J (2012) Models of electrical activity: calibration and prediction testing on the same cell. *Biophys J* 103(9):2021–2032. doi:[10.1016/j.bpj.2012.09.034](https://doi.org/10.1016/j.bpj.2012.09.034)
- Toth BA, Kostuk M, Meliza CD, Margoliash D, Abarbanel HDI (2011) Dynamical estimation of neuron and network properties I: variational methods. *Biol Cybern* 105:217–237. doi:[10.1007/s00422-011-0459-1](https://doi.org/10.1007/s00422-011-0459-1)
- Trimmer J, Rhodes K (2004) Localization of voltage-gated ion channels in mammalian brain. *Annu Rev Physiol* 66(1):477–519. doi:[10.1146/annurev.physiol.66.032102.113328](https://doi.org/10.1146/annurev.physiol.66.032102.113328)
- Vanier MC, Bower JM (1999) A comparative survey of automated parameter-search methods for compartmental neural models. *J Comput Neurosci* 7(2):149–171. doi:[10.1023/A:1008972005316](https://doi.org/10.1023/A:1008972005316)

- Vavoulis DV, Straub VA, Aston JAD, Feng J (2012) A self-organizing state-space-model approach for parameter estimation in Hodgkin–Huxley-type models of single neurons. *PLoS Comput Biol*. doi:[10.1371/journal.pcbi.1002401](https://doi.org/10.1371/journal.pcbi.1002401)
- Wächter A (2002) An interior point algorithm for large-scale nonlinear optimization with applications in process engineering. Phd thesis, Carnegie Mellon University
- Wolpert DH, Macready WG (1997) No free lunch theorems for optimization. *IEEE T Evolut Comput* 1(1):67–82